RICE UNIVERSITY

Single-Walled Carbon Nanotube Dynamics in Simple and Complex Media

by

Nikta Fakhri

A Thesis Submitted
in Partial Fulfillment of the
Requirements for the Degree

Doctor of Philosophy

Approved, Thesis Committee:

Matteo Pasquali, Chair
Professor of Chemical and Biomolecular Engineering

Cecilia Clementi
Professor of Chemistry

Laurent Cognet
CNRS Research Associate, University of Bordeaux, France

Fred C. MacKintosh
Professor of Physics, Free University, The Netherlands

Robert M. Raphael
Associate Professor of Bioengineering

R. Bruce Weisman
Professor of Chemistry

Houston, Texas
June, 2010

RICE UNIVERSITY

Single-Walled Carbon Nanotube Dynamics in Simple and Complex Media

by

Nikta Fakhri

A THESIS SUBMITTED
IN PARTIAL FULFILLMENT OF THE
REQUIREMENTS FOR THE DEGREE

Doctor of Philosophy

APPROVED, THESIS COMMITTEE:

Matteo Pasquali, Chair
Professor of Chemical and Biomolecular Engineering

Cecilia Clementi
Professor of Chemistry

Laurent Cognet
CNRS Research Associate, University of Bordeaux, France

Fred C. MacKintosh
Professor of Physics, Free University, The Netherlands

Robert M. Raphael
Associate Professor of Bioengineering

R. Bruce Weisman
Professor of Chemistry

Houston, Texas
June, 2010

ABSTRACT

Single-Walled Carbon Nanotube Dynamics in Simple and Complex Media

by

Nikta Fakhri

Understanding the dynamics of single-walled carbon nanotubes (SWNTs) in simple and complex environments is crucial for establishing potential application of nanotube architectures for materials and biosciences. In this thesis we employ the visualization and analysis tools to image and quantify and the Brownian bending and diffusion of SWNTs in different media in order to understand and eventually to tailor nanotube mobility in confined environments.

We image Brownian bending dynamics of SWNTs in water using Near-infrared (NIR) fluorescence microscopy. The bending stiffness of each chirality-assigned SWNT is extracted from the variance of the curvature fluctuations. Relaxation times of the bending fluctuations are measured from the autocorrelation of SWNT shapes. We find that the bending stiffness scales as the cube of the nanotube diameter, in agreement with an elastic continuum model. The measured shape relaxation times are in excellent agreement with the semiflexible chain model, showing that SWNTs may truly be considered as the ideal model semiflexible filaments.

The motion of stiff objects in crowded environments has been investigated for more than three decades in polymer science and biophysics; yet, theory and experiments have not established whether a minute amount of flexibility affects the mobility of stiff slender filaments. We image the Brownian motion of SWNTs in a network by

NIR fluorescence microscopy. We show direct evidence of SWNTs reptating in the network, and confirm that their small flexibility enhances significantly their rotational diffusion. Our results establish the reptation dynamics of stiff filaments and provide a framework to tailor SWNTs mobility in confined media.

By varying SWNT surface modifications, we can selectively tune the sensitivity of the carbon nanotubes to the different physical properties of the porous media for sensing applications. We introduce a simple procedure for dispersion of SWNTs in aqueous solutions using triblock copolymer, PS-*b*-P2VP-*b*-PEO. This process yields stable dispersions of individual SWNTs without a need for ultracentrifugation, thus increasing nanotube yield. We show that the SWNT suspension is stable under a wide pH range as well as high salinity environments. These stable suspensions can be used in a wide range of applications in different media where stability is crucial.

Contents

Illustrations

Chapter 1

Introduction

1.1 Polymer dynamics

The dynamics of a filament of stiff material with nanoscale diameter and microscale length embedded in a viscous medium is essentially dominated by the balance of Brownian forces, which tend to bend the filament, and elastic forces, which oppose this curvature. The simplest model of such filament is that of an inextensible elastic beam with bending stiffness $\kappa = EI$, where E is the elastic modulus and I the moment of inertia of the filament about its axis; the ratio of bending stiffness and thermal energy yields a characteristic length, termed persistence length $L_p = \kappa/k_BT$, where k_B is Boltzmann constant and T is absolute temperature [1]. This is the characteristic lengthscale over which the filament shows significant curvature induced by thermal fluctuations. The variation in the orientation of the tangent vectors along the contour of the filament provides a geometrical interpretation of the persistence length. Consider the scalar product of the unit tangent vectors $\mathbf{u}(0) \cdot \mathbf{u}(s)$, which has its maximum value of unity only if the tangent vectors are parallel at arclength distances. At non-zero temperature, the filament samples a variety of orientations such that the ensemble average $\langle \mathbf{u}(0) \cdot \mathbf{u}(s) \rangle$ has a maximum absolute value of unity. The quantity $\langle \mathbf{u}(0) \cdot \mathbf{u}(s) \rangle$ is referred to as the correlation function of the tangent vector: it describes the correlation between the direction of the tangent vectors at different positions along the curve. Thus, the persistence length measures the distance

along the filament above which the orientation of the curve becomes uncorrelated. For a three-dimensional angle change:

$$\langle \mathbf{u}(0) \cdot \mathbf{u}(s) \rangle \equiv \cos\theta(s) = e^{-s/L_p} \tag{1.1}$$

whereas for a filament constrained to a plane, the decay length doubles:

$$\langle \cos\theta(s) \rangle = e^{-s/2L_p} \tag{1.2}$$

Polymers are normally classified as flexible ($L > L_p$), semiflexible ($L \sim L_p$), or stiff ($L < L_p$) depending on how effectively Brownian motion randomizes their shape. Recent advances in visualization techniques and availability of polymer model systems that can be visualized on length-scales accessible to optical microscopy permit to observe single polymers of a network and determine how the behavior of individual components of a network determines the macroscopic properties of the polymeric system. For flexible polymer and semiflexible polymers, fluorescently labeled DNA [2] and actin [3] have been used as the model systems to test the basic postulates and predictions of polymer dynamics in both dilute and concentrated solutions.

However, so far there has not been such a counter part for the limit of stiff polymers and it has been hard to test polymer theories directly against experiments. The question of stiff filaments dynamics has great relevance in biophysics, dynamics of rod-like polymer solutions and melts, as well as the emerging field of carbon nanotubes soft condensed matter, which has great importance for applications.

1.2 SWNT as a model stiff polymer

Single-walled carbon nanotubes (SWNTs) are high aspect ratio tubular structure of all carbon that are classified as polymers. Despite having diameters comparable to synthetic polymers, they are extremely stiff and show mechanical resistance

to bending. A SWNT structure can be conceptualized by rolling a graphite sheet into a seamless cylinder. This rolling up process generates a large number of discrete transverse structures can uniquely be identified by two integers (n,m) which differ in tube diameter and roll-up angle (chirality). SWNT electronic structure is governed by transverse structure. About two-third of SWNTs (in which n m does not divide evenly by 3) are semiconductors with bandgaps that vary approximately inversely with nanotube diameter. Remarkably, aqueous samples enriched in individual surfactant-stabilized semiconducting SWNTs display near-infrared photoluminescence [4]. Each near-infrared emission wavelengths has been assigned to specific (n,m) assignment [5], so the emission of each (n,m) can be directly visualized using a liquid nitrogen-cooled camera equipped with a near-infrared detector [6].

In this thesis I utilize SWNTs as the ideal model systems of stiff polymers to address important open problems in polymer physics by bridging the gap between the theory and single molecule experiments.

1.3 Overview of thesis

In **chapter 2**, we studied the bending dynamics of individual SWNTs in water. We exploited the intrinsic near-infrared fluorescence of semiconducting SWNTs to image individual nanotubes as they undergo Brownian motion. The bending rigidity (persistence length) of each SWNT was determined from the amplitude of thermally induced fluctuations. Persistence length was found to scale with the cube of diameter, with values between $\sim$ 20 to 100 microns. We also found that the thermal shape fluctuations of SWNTs accurately follow the semiflexible (stiff) filament model. There has been much recent activity and interest in stiff polymers, largely motivated by biopolymers. But, so far, there has been no way of designing/controlling the mechanics of

the fibers/polymers. This work introduced a system of filaments with variable stiffness. Since the persistence length is the most important microscopic parameter for most of the material properties of semiflexible gels, this study opens up new avenues for fundamental studies of such gels. In addition, the varying persistence lengths within the family of SWNT structures could be exploited to develop rod-like nano and microscale probes for microrheological studies of complex fluids and biological systems and to tailor nanotube mobility in confined environments such as living cells and tissues. The effect of persistence length on mobility is the topic of next chapter.

In **chapter 3**, we showed the reptation motion of individual SWNTs in agarose gel and elucidated the effect of finite flexibility on rotational and translational motion. By using NIR fluorescence microscopy, we quantified the dependence of SWNTs mobility on physical parameters such as SWNTs stiffness and length as well as network pore sizes. Our results strongly indicated the finite flexibility of stiff threads results in an enhanced rotational and translational diffusion in agreement with Odijk's theory and inconsistent with Doi's scaling of rotational diffusion for a rigid rod. Our observations provide insight into reptation dynamics of stiff polymers as well as a framework to tailor SWNTs mobility in confined environments. By varying SWNT surface modifications, we can selectively tune the sensitivity of the carbon nanotubes to the different physical properties of the porous media for sensing applications. SWNT surface modifications is the topic of next chapter.

In **chapter 4**, we introduced a simple procedure for dispersing as-produced SWNTs in aqueous solutions of triblock copolymer, poly(Styrene)-*b*-(2-Vinyl Pyridine)-*b*-(Ethyelne Oxide) (PS-*b*-P2VP-*b*-PEO). Entropic repulsion among the absorbed polymer chains generates a free energy barrier that prevents SWNTs from approaching the attractive part of the intertube potential. Consequentially, stable dispersions of

individual SWNTs in aqueous media can be prepared which requires no centrifugation and thus material is conserved. We used this SWNT-triblock copolymer system to study the effect of pH and salinity on polymer micelle conformations. We also described the ability of the SWNT-triblock copolymer assembly in sequestering hydrophobic molecules at very fast rates.

Chapter 2

Bending dynamics of SWNTs in liquids

Understanding the dynamics of single-walled carbon nanotubes (SWNTs) in fluids is crucial for establishing potential application of nanotube architectures for materials and biosciences. Theoretical models have predicted that SWNTs in fluids should behave essentially as stiff rods. Here we study the bending dynamics of individually suspended SWNTs in water at thermal equilibrium using near-infrared fluorescence microscopy. The bending stiffness of each chirality-assigned SWNT is extracted from the variance of the curvature fluctuations induced by Brownian motion. The relaxation times of the curvature fluctuations are measured from the autocorrelation of each SWNT shape. We find that the bending stiffness scales as the cube of the SWNT diameter, in agreement with an elastic continuum model; intriguingly, such bending stiffness gives a persistence length comparable to that of actin and microtubules. The measured shape relaxation times are in excellent agreements with the semiflexible chain model developed for actin, showing that SWNTs may truly be considered as the archetypal semiflexible filaments. These findings are a major step towards exploiting the properties of SWNTs in biological applications, particularly those requiring the motion of SWNTs in confined spaces such as the intracellular matrix, where diffusivity is expected to depend strongly on stiffness, as well as rod-like probes for microrheology, where the tunable bending stiffness could be used to probe materials on different timescales.

2.1 Introduction

The dynamics of a filament of stiff material with nanoscale diameter and microscale length embedded in a viscous medium are essentially dominated by the balance of Brownian forces, which tend to bend the filament, and elastic forces, which oppose this curvature. The simplest model of such filament is that of an inextensible elastic beam with bending stiffness $\kappa = EI$, where E is the elastic modulus and I the moment of inertia of the filament about its axis; the ratio of bending stiffness and thermal energy yields a characteristic length, termed persistence length $L_p = \frac{\kappa}{k_B T}$, where k_B is Boltzmann constant and T is absolute temperature [1]. This is the characteristic lengthscale over which the filament shows significant curvature induced by thermal fluctuations. Hence, *short* filaments ($L_p < L$) essentially appear as rigid rods, whereas *long* filaments $L_p > L$ display significant bending.

Single-walled carbon nanotubes (SWNTs) are tubular nanostructures of covalently bonded carbon atoms, with typical diameters near 1 nm and lengths in the micrometer range. Their remarkable combination of very large aspect ratios, high mechanical strength, and versatile electronic properties makes SWNTs highly suited for many applications, e.g., in material engineering, soft matter science, and biomedicine [7, 8]. However, advances in applications are presently limited by scant fundamental understanding of their mechanical and dynamical behavior in fluid environments.

SWNT persistence length is important in a variety of applications such as organization on patterned surfaces [9], the ability to form liquid crystals [10], and the stiffening of polymeric networks [11, 12]. Various methods have been used to infer or measure the persistence length of SWNTs. There is still controversy on whether, in the absence of flow, individual SWNTs in liquids should be considered rigid $L_p >> L$ or semi-flexible $L_p \sim L$: persistence length measurements based on the size of closed

SWNT rings estimated a persistence length of 800 nm [13]; experimental data using neutron scattering indicated that SWNTs behave as rigid rods on length scales of at least $\sim$ 150 nm [14], whereas X-ray scattering data suggested that SWNT do not display rod-like behavior at any length [15]. Fluorescence video microscopy of fluorescently labeled SWNTs estimated that SWNT persistence length ranges between 32 and 174 μm; however, it was not possible to differentiate between individual SWNTs and small bundles using this method [16].

Theoretically, the bending stiffness of SWNTs has been calculated based on a continuum model for a hollow cylinder of radius R as $\kappa = \pi C R^3$; the in-plane stiffness $C \sim 345 J/m^2$ was determined by measuring the elastic energy under axial strain using MD simulations of a plane graphene sheet [17, 18]. This model suggests that bending stiffness, and hence persistence length should depend on the SWNT diameter; however, there is no experimental evidence of such relationship.

Using fluorescence microscopy to measure directly the shape fluctuations of individual filaments is a powerful tool to study the mechanical behavior of one-dimensional nano-objects; variations of this technique have been used to measure the bending stiffness of biopolymers such as actin and microtubules [19–22]. Here we use fluorescence video-microscopy in the near-infrared region to image directly SWNTs undergoing Brownian motion in a quasi-two-dimensional chamber.

2.2 Materials

SWNTs with diameters between 0.7 and 1.2 nm were obtained from HiPco reactor (batches no. 125.2, 161.1, 162.5). Dilute aqueous suspensions of SWNTs (1-10 ng/mL) in SDBS (sodium dodecylbenzenesulfonate, 1 % wt) were prepared by mild ultra-sonication (7 W, 5-6 s) to minimize SWNT breaking. Suspended SWNTs were

imaged [6, 23] in a quasi-two-dimensional chamber $\sim 1.0 \pm 0.5$ μm thick made by sandwiching ~ 0.7 μL of sample (1.0 μL for samples with higher viscosity) between a microscope slide and coverslip. The sample was sealed with vacuum grease to prevent convective flow due to evaporation. Enough time was allowed between sealing of the sample and image acquisition to ensure the cessation of any convective flow induced during sample preparation. All experiments were performed at room temperature.

To slow down the SWNT dynamics for bending-mode relaxation analysis, the sample viscosity was increased by adding a mixture of 60/40 sucrose and glucose solution (40 total sugar by mass) and 1 % wt SDBS to the SWNT suspension (1 μL of SWNTs suspension to 10 μL of viscous solution) to yield a final viscosity of ~ 13 mPa s.

2.3 Experimental setup

The use of intrinsic fluorescence provides three benefits. First, because nanotubes are imaged using their own characteristic emission rather than that of an added fluorophore, all observed objects are confidently identified as SWNTs. Second, aggregation of SWNTs into bundles strongly quenches the emission, so there is good discrimination against nanotube bundles. Finally, the wavelength of a nanotube's near-infrared fluorescence is characteristic of its exact transverse structure [5], so spectral analysis reveals individual SWNT diameters.

2.3.1 Microscopy

NIR-fluorescence microscopy offers the advantages of image acquisition and parallel spectra detection for individually suspended semiconducting SWNTs [6]. The sample, mounted on a translational stage of a Nikon TE-2000 inverted microscope, is excited

with a 660 nm or 785 nm external diode laser. The laser beam is passed through a polarization cube and a quarter wave-plate to achieve circularly polarized light.* The beam is then focused on the sample through an aspheric lens † The emission is collected with a Nikon 100x oil-immersion objective (N.A. 1.4). The collected light consists of both excitation and emission wavelengths. A dichroic beam splitter in series with a dielectric long-pass filter (cut wavelength of 946 or 1125 nm) blocks the excitation wavelengths. An Indigo Alpha NIR InGaAs camera (320 $\times$ 256 pixels) acquires frames with 10-50 ms exposure times. The camera is sensitive from 900 to 1600 nm. The depth of focus for the system is about 0.5 μm. Figure 2.1 shows the thermal undulations of a SWNT visualized by this technique.

Diffraction limits the resolution of SWNT dimensions in the radial direction. The estimated resolution of this system is approximately 1 μm.

2.3.2 Spectroscopy

The spatially resolved emission spectra of the SWNTs are collected with a J-Y C140 spectrograph with a cryogenically cooled 512-element InGaAs array at its focal plane. The spectrograph is connected to a second output port of the microscope. The spectrum of the nanotube is acquired by moving it to a specific region in observation field, focusing the beam with the aspheric lens on that region and switching to the spectrograph port. The spectra is averaged over 10 exposures of 20 s (figure 2.2).

During the experiments, we found some tubes with emission peaks that were shifted considerably and some unassigned tubes. For the purpose of our measurements

---

*The excitation beam's polarization axis can be changed by rotation of a half-wave retardation plate.

†Aspheric lens (f=18.4mm) changes the size of the illumination area.

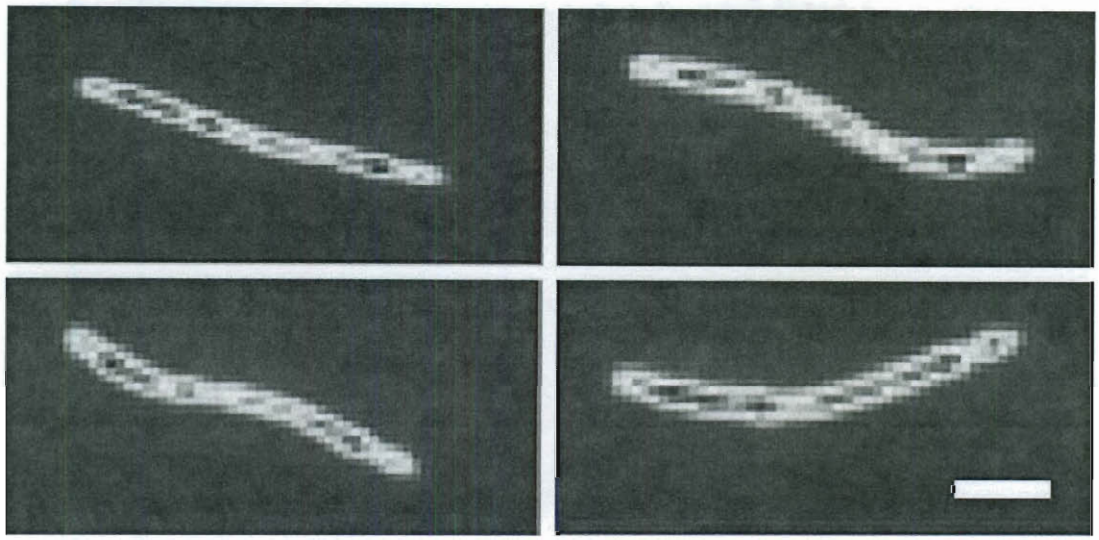

Figure 2.1 : Representative near-infrared (false colored) fluorescence images of the same SWNT in liquid suspension illustrating Brownian bending deformations (Scale bar, 2μm)

we did not use these nanotubes and the maximum shift acceptable in assigning a nanotube was 2 nm.

2.4 Data acquisition

For each SWNT, a movie of 1000 frames were recorded with exposure times 10-50 ms. After image acquisition the spectrum of that nanotube was acquired. The spectra is averaged over 10 exposures of 20 s. The (n,m) assignment of the SWNT is deduced

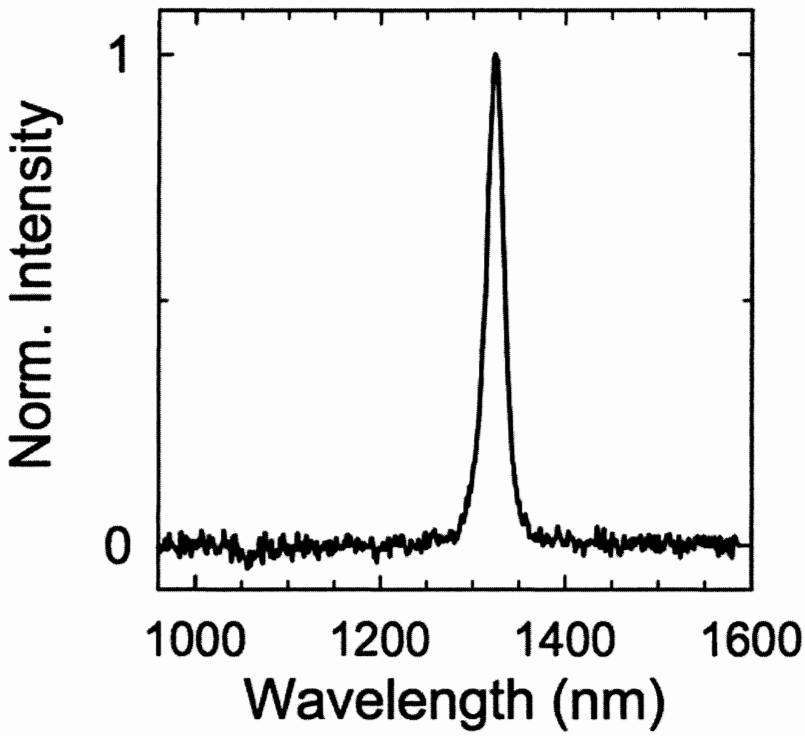

Figure 2.2 : Individual SWNT emission spectrum with peak at 1323 nm implying a (9,7) structure, with a diameter of 1.09 nm

from the single peak spectrum and the diameter (nm) was calculated:

$$d = \frac{1.42\sqrt{3(m^2 + mn + n^2)}}{\pi} \tag{2.1}$$

The shallow cell depth limits the SWNTs movements to only two dimension. 25°C is the assumed temperature throughout the experiment.

2.5 Image analysis

2.5.1 Image digitization

The images were processed by a custom software written in Matlab. In order to get the backbone of the nanotube in each image, first the standard image processing technique Skeletonization in Matlab were used. However because of the resolution limitation of NIR microscopy the deflection to pixelation error were high and a lot of information (bending and deflection) would be discarded. To overcome this problem a custom technique has been developed. The average and standard deviations of the intensity of each image were computed. Linear combinations of the average and the standard deviation is used to threshold the SWNT from the background. The position of each SWNT in its frame is recognized (the cosine of the angle with x-axis). Knowing the position, the coordinates of the backbone of the SWNTs were determined with an intensity-weighted center-of-mass method: A two-dimensional fixed area kernel moved along the contour of the nanotube in the original image with a one-pixel step size. By measuring the center of intensity for each position of the kernel, the real-space coordinates of that point on the backbone were extracted to obtain a full set of SWNT backbone coordinates $(x_i, y_i))$ (figure 2.3).

2.5.2 Shape analysis

The bending rigidity (persistence length) of each individual SWNT can be determined from the amplitude of the shape fluctuations [20, 24].

Following the procedure developed by Gittes et al. [20], the shape (tangent angle) of the nanotube ($\theta(s_i) = tan^{-1}\left(\frac{y_{i+1}-y_i}{x_{i+1}-x_i}\right)$) was calculated from the backbone

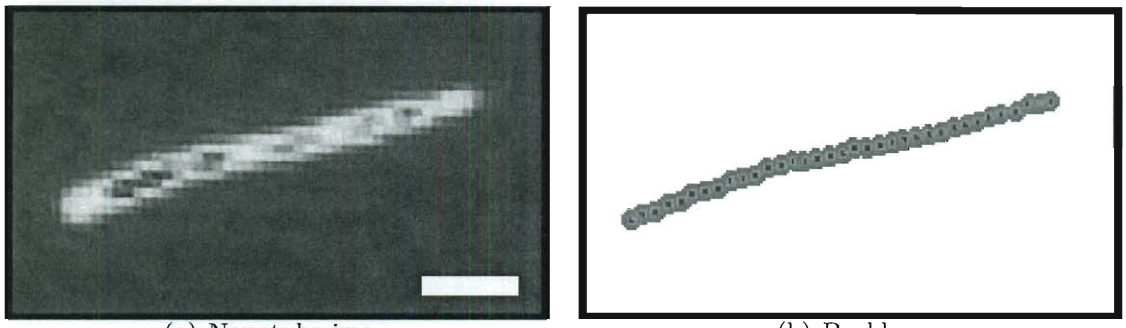

(a) Nanotube image (b) Backbone

Figure 2.3 : Fluorescence image of the nanotube and corresponding coordinates

coordinates and decomposed into Fourier modes:

$$\theta(s) = \sqrt{\frac{2}{L}} \sum_{n=0}^{\infty} a_n \cos\left(\frac{n\pi s}{L}\right) \tag{2.2}$$

where n is the mode number, a_n the mode amplitude, and L the SWNT contour length. The amplitude of each mode was extracted by taking the Fourier inverse of this equation:

$$a_n = \sqrt{\frac{2}{L}} \int_0^L ds\theta(s) \cos\left(\frac{n\pi s}{L}\right) \tag{2.3}$$

In the absence of external forces, equipartition theorem dictates that the variance of the amplitude of the bending modes is inversely proportional to the bending rigidity:

$$var(a_n) = \frac{k_B T}{\kappa} \left(\frac{L}{n\pi}\right)^2 \tag{2.4}$$

where the angular brackets denote ensemble average or average over time, since the system is ergodic.

The random noise due to limited resolution and thus error in SWNTs localization

follows the equation:

$$\langle a_n^2 \rangle^{noise} = \frac{4}{L}\epsilon^2 \left[1 + (N-1)\sin^2\left(\frac{n\pi}{2N}\right)\right] \tag{2.5}$$

where ϵ is the RMS error of SWNTs backbone localization.

The outline of the developed code is as follows:

- Using the $N+1$ digitized points, we derive the length and tangent angles for the N segments:

$$\triangle s_i = [(x_{i+1} - x_i)^2) + (y_{i+1} - y_i)^2)]^{1/2} \tag{2.6}$$

$$u_i = \tan^{-1}[(y_{i+1} - y_i)/(x_{i+1} - x_i)] \tag{2.7}$$

- The inverse Fourier transform is computed using the approximation (for n = 1 to $N+1$):

$$a_n = \sqrt{\frac{2}{L}} \sum_{i=1}^{N} u_i \triangle s_i \cos(\frac{n\pi}{L} s_i^{mid}) \tag{2.8}$$

where $L = \sum_{i=1}^{N} \triangle s_i$ and $s_i^{mid} = \triangle s_1 + \triangle s_2 + \ldots + \triangle s_{i-1} + 1/2 \triangle s_i$.

- The variance of the each mode amplitude (n) over all frames is computed:

$$var\,(a_n) = \frac{1}{L_p}\left(\frac{L}{n\pi}\right)^2 \tag{2.9}$$

2.5.3 Dynamics analysis

The cosine modes are not exactly normal modes for the dynamics of semiflexible filaments with free ends [19, 25], yet their dynamics is well-approximated by single-exponential relaxation, and the relaxation times can be extracted from the autocorrelation of mode amplitudes:

$$\langle a_n\,(t + \Delta t) \cdot a_n\,(t) \rangle = |a_n\,(t)\,a_n\,(t)\,| e^{\frac{-\Delta t}{\tau_n}} \tag{2.10}$$

It can be shown that the mode relaxation times τ_n are given by [20, 26]:

$$\tau_n \approx \frac{\gamma}{\kappa q^4} \tag{2.11}$$

Here $q = \left(n + \frac{1}{2}\right)\pi/L$ and the hydrodynamic friction coefficient γ for a rod of length L and diameter d confined in a gap comparable to L can be approximated as twice the bulk friction coefficient, $\gamma \approx 4\pi\eta/ln\,(L/d)$ where η is the bulk viscosity [27].

2.6 Results

We analyzed 34 nanotubes with diameters between 0.7 to 1.2 nm. Measurements were restricted to nanotubes with length greater than 3 μm to minimize the effects of pixilation and diffraction. We used only SWNTs which showed identical emission profiles in different sections of their backbone, indicating the absence of significant structural defects (e.g.,chirality switch) or bundling with other nanotubes. In a typical analysis, 1000 images of a SWNT were acquired. The backbone coordinates of the SWNTs were obtained with sub-pixel accuracy by intensity weighting. Following the procedure by Gittes et al. (see(2.5)), the shape of the SWNT in each image was expressed as a sum of cosine modes which form an orthogonal basis, and the amplitude of these bending modes were extracted by projecting the image shape onto the cosine modes themselves.

Figure 2.4 shows the variance of the amplitude of each of the bending modes against the mode number. The measured mean is essentially zero, showing that these SWNT have no static curvature. The longer wavelength modes (low n) show the expected n^{-2} dependence of amplitude vs. mode number , indicating that the measured variance is due to thermal fluctuations; the n^{-2} dependence breaks down at higher modes (typically $n > 5$) because of the effect of pixilation and diffraction,

the estimated variance contributed by experimental noise is shown by blue triangles and black continuous line which follows equation (2.5).

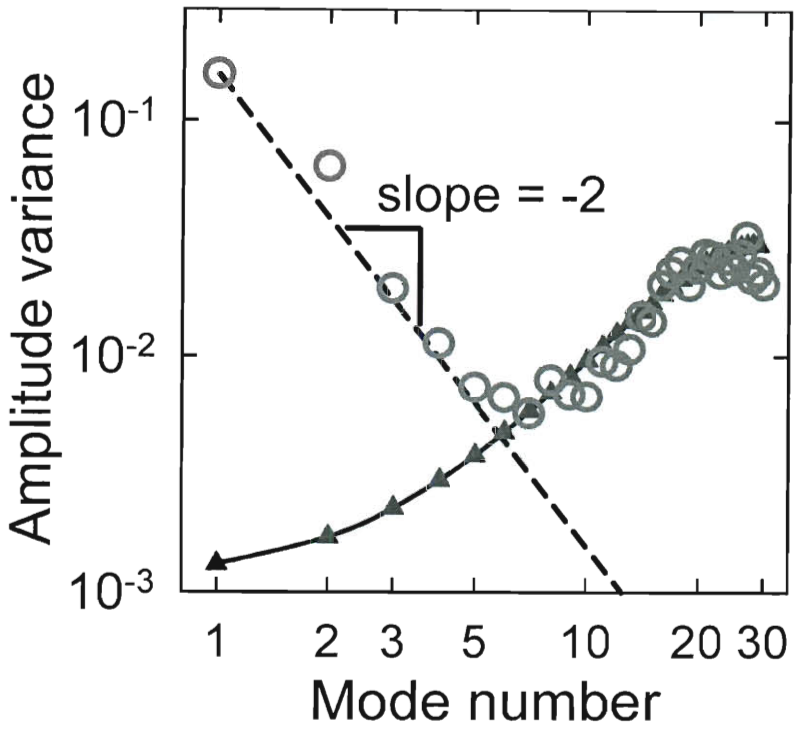

Figure 2.4 : Variance (in μ m) of the amplitude of the bending modes for the (9,7) nanotube vs. mode number

The analysis of mode amplitudes provides a test of internal consistency: for example, any local structural defect in nanotube structure should yield a locally lower stiffness, which would increase the amplitudes of specific modes, breaking the n^{-2} decay law; we observe no anomalies in the plots of mode amplitude vs. mode number, which suggests the absence of significant mechanical defects in the studied nanotubes.

Figure 2.5 shows how SWNT persistence length (or bending stiffness) depends on SWNT diameter. The measured values of range from 26 μm to 138 μm. The measured bending stiffness scales with the cube of diameter, as predicted by the

elastic continuum model [17], $\kappa = \pi C R^3$, with best fit $C = 678 \pm 22\ J/m^2$ for the in-plane stiffness. However, the theoretical continuum model underestimates the experimental data by approximately a factor of two [17].

When electrostatic repulsions between the charges along the filament in aqueous solutions are not screened, they will tend to make the local rigidity larger. The total persistence length $L_p^{charged}$ would represent the effective rigidity of the filament as the sum of two contributions: the intrinsic persistence length L_p of the corresponding uncharged filament and the electrostatic persistence length $L_{electrostatic}$, which would depend on the screening, i.e., on ionic strength due to external charges:

$$L_p^{charged} = L_p + L_{electrostatic} \tag{2.12}$$

In the Odijk-Skonick-Fixman (hereafter called OSF) theories [28,29], the charged filament is described by a semiflexible chain near the rod limit having N charged monomers separated by a distance A along its contour. The electrostatic interaction between the charged segments is assumed to be given by the Debye-Huckel potential, $v(r) = l_B e^{-l_D r}/r$. The strength of the interaction is measured in terms of the Bjerrum length $l_B = e^2/4\pi\epsilon k_B T$ where e is the charge per segment, and ϵ is the dielectric constant of the solvent. The Debye screening length, l_D, is the distance beyond which the electrostatic interaction is screened. It depends on the total concentration, n, of the counterions (assumed to be monovalent) and any added electrolytes through the relation $l_D^{-1} = 4\pi l_B n$. OSF calculated the increase in free energy due to electrostatic interaction and elastic bending energy for a slightly bent configuration with reference to a rodlike configuration. This was used to analyze the effect of the charges on the chain stiffness, leading naturally to the concept of the electrostatic persistence length. Following Odijk, the configuration of the filament is described by the unit tangent vector $\mathbf{u}(s) = \frac{\partial \mathbf{r}}{\partial s}$. If the chain is near the rod limit, only those paths which

minimize the elastic free energy paths, i.e. paths for which the angle θ defined by $\cos(\theta(s)) = \mathbf{u}(s).\mathbf{u}(0)$ varies linearly with s, contribute significantly to the partition function. The electrostatic contribution to the chain stiffness due to the departure from the rod limit allows for the calculation of $l_{electrostatic}$, which in the limit of $l_D^{-1}L >> 1$ is given by:

$$l_{electrostatic} = \frac{l_B l_D^2}{4A^2} \equiv l_{OSF} \tag{2.13}$$

In our experiments the Debye screening length is about 1.7 nm and Bjerrum length is 0.7 nm. A the distance between charges depends on the surface coverage of surfactant on nanotubes. Assuming $A = 1.848$ nm as lower bound for A (length of the C-C chain in SDBS), the upperbound for $l_{electrostatic}$ will be very small and thus we rules out any stiffening effect from the ionic surfactant that coats the nanotubes.

The persistence length measurements normalized by the diameter cubed are plotted against length (figure 2.6(a)), show no statistically significant correlation between persistence length and SWNT length (correlation coefficient ~ 0.022), as one would expect in such systems. There is also no apparent correlation between persistence length and SWNT chirality (figure 2.6(b)).

Fourier modes provide a basis that captures well the instantaneous as well as dynamical SWNT shape. The relaxation times of the SWNTs can be extracted from the exponential decay of the autocorrelation of the amplitude of the Fourier modes, as described in the methods section. Long exposure times relative to the relaxation time can blur the filament motion and depress the apparent shape fluctuations, thereby hampering the interpretation of filament dynamics. To minimize this source of error, the dynamics of nanotubes were slowed down by raising the solvent viscosity with a mixture of sucrose and glucose.

Figure 2.7 shows the decay of the autocorrelation of typical SWNT shapes (first

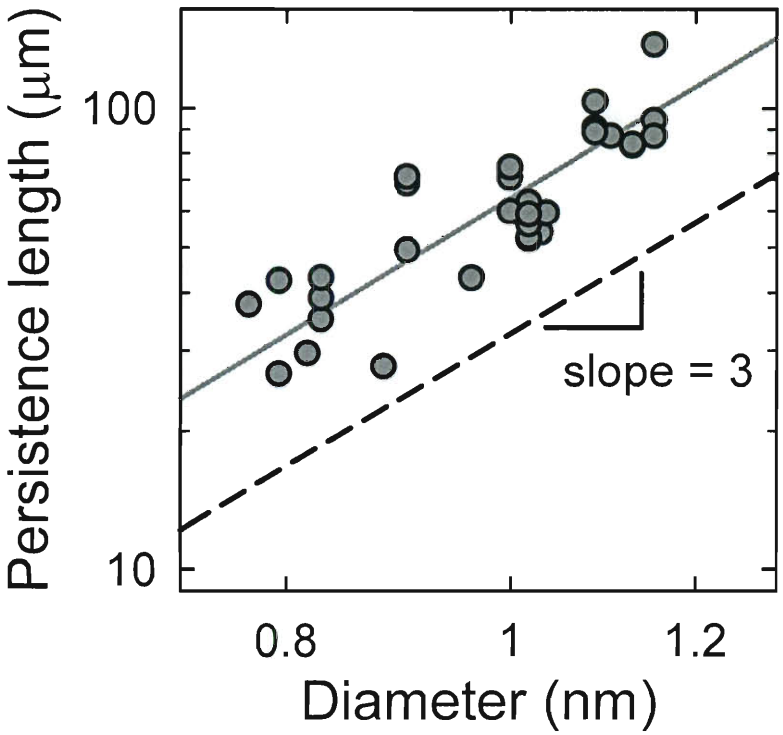

Figure 2.5 : Persistence length of SWNTs as a function of their diameters

and second mode), which essentially decay as single exponential [19]; data acquired with different exposure times overlap, indicating that the image acquisition rate is sufficiently fast to capture the dynamics. Because all other parameters (fluid viscosity, temperature, and SWNT length) are known independently, the persistence length of each SWNT can be extracted from the dynamic data by using the theoretical relationship [25,26,30] between persistence length and bending relaxation times $L_p \approx \gamma/\tau_n k_B T \left((n+1/2)\,\pi/L\right)^4$, , where γ is the friction coefficient and τ_n is the relaxation time of mode n. Persistence length values extracted from the relaxation times of the first bending mode of four SWNTs are in excellent agreement with equilibrium measurement (figure 2.8). Such agreement is remarkable, considering the simplified

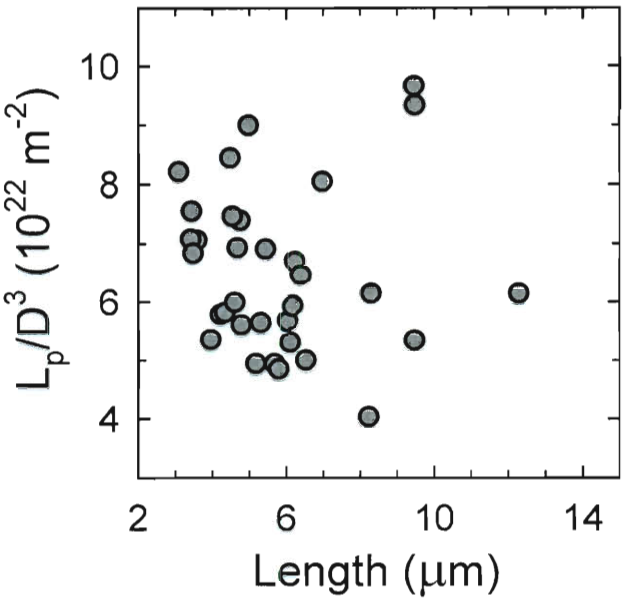

(a) Length

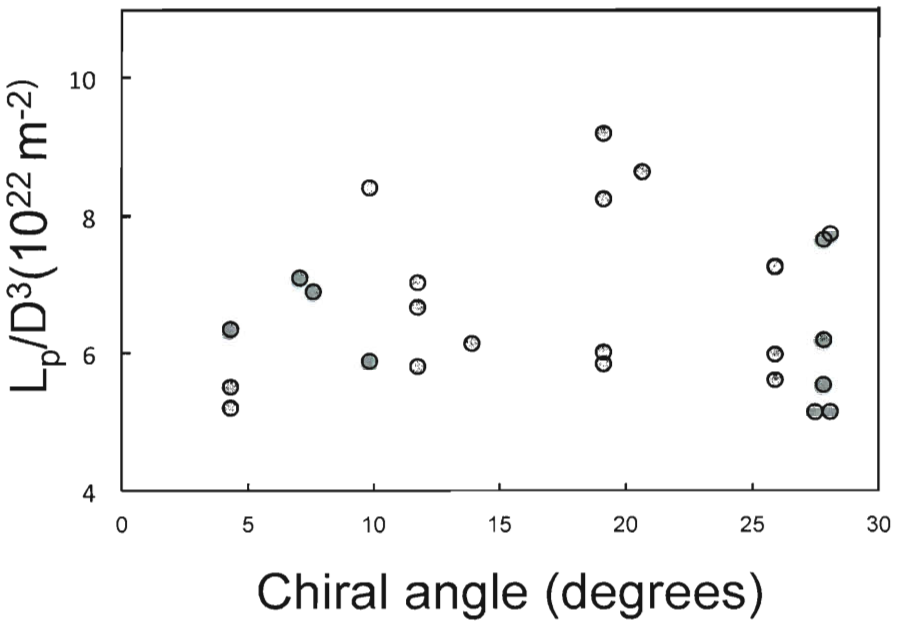

(b) Angle

Figure 2.6 : Persistence length of SWNTs normalized by the diameter cubed plotted vs. the length and chiral angle

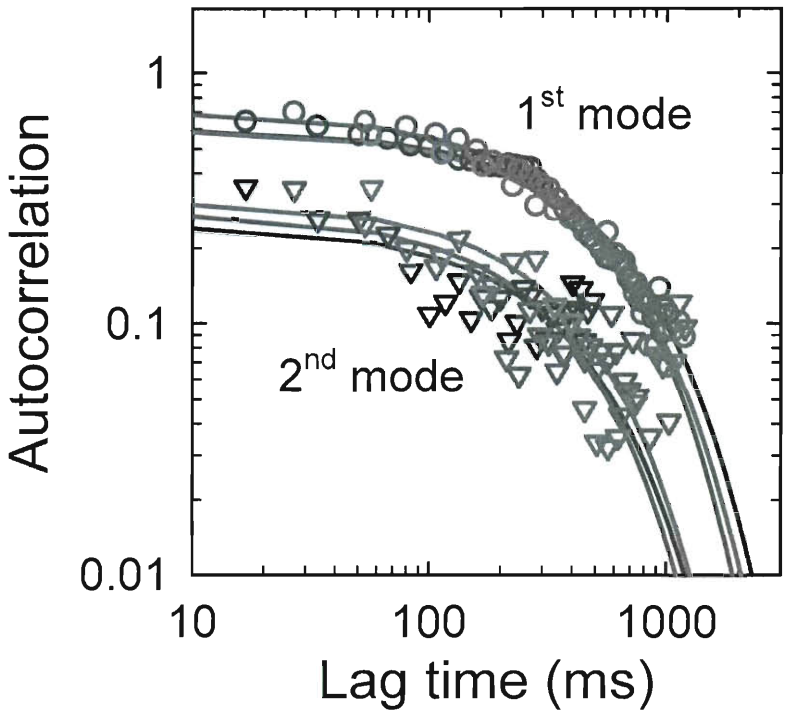

Figure 2.7 : Shape autocorrelation data for the first bending mode (circles) and second bending mode (triangles) of a nanotube as calculated from image sequences with exposure times of 10, 20, and 50 ms (blue, green, and red, respectively). Solid lines of the same color show corresponding exponential decay best fits

nature of the semiflexible chain model.

2.7 Discussion

In summary, we have studied the Brownian bending dynamics of diameter-resolved SWNTs in ordinary aqueous surfactant suspensions. The measured persistence lengths range from 26 μm to 138 μm for SWNTs of diameter from 0.77 to 1.15 nm. Persistence length is found to scale with the cube of diameter, as expected from an elastic continuum model [17], but the deduced nanotube stiffness significantly exceeds a the-

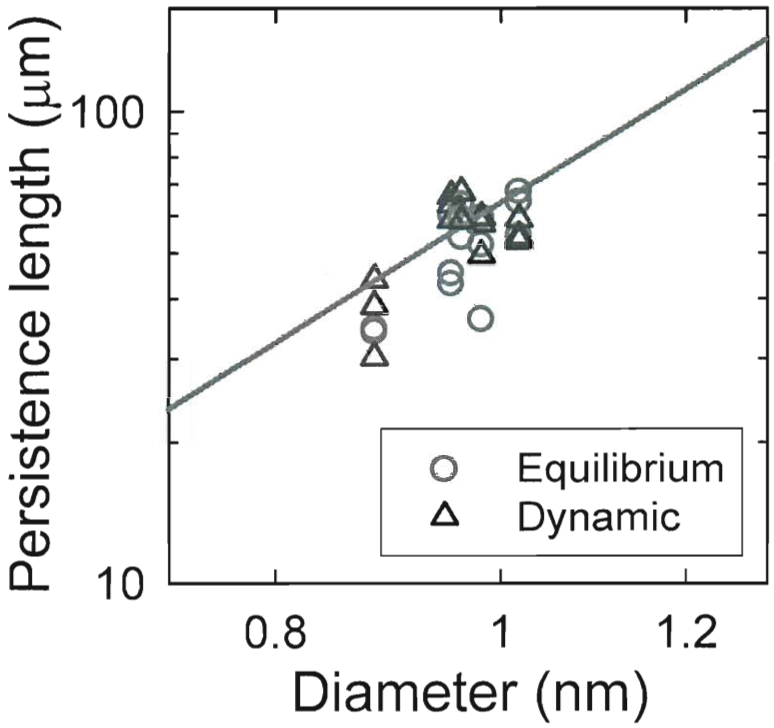

Figure 2.8 : Persistence length comparisons for five nanotubes as determined by using equilibrium bending analysis (red circles) and bending mode relaxation analysis (blue triangles) of the first bending mode for exposure times of 10, 20 and 50 ms

oretically predicted value. Smaller values of persistence length reported in previous studies might reflect the presence of other forces in addition to Brownian ones, such as the intertube van der Waals attractions that control the structure of buckypaper [18]. The persistence length of a SWNT within our diameter range is comparable to that of actin filaments ($\sim$ 17 μm) but somewhat shorter than that of microtubules (on the order of millimeters) because the higher elastic modulus of the SWNTs is counterbalanced by larger diameters of actin ($\sim$ 7 nm) and microtubules ($\sim$ 25 nm).

Interestingly, based on the scaling of persistence length with CNT diameter, SWNTs should be several orders of magnitude less stiff than their multi-walled coun-

terparts [18] (MWNTs, diameter 10-50 nm). The ultimate mesoscopic and macroscopic properties of functional materials such as fibers are dictated by the behavior of the constituent single molecules [18, 31]. Understanding the relationship between single molecule mechanics and the collective properties of their macromolecular assemblies has implications for the rational design of carbon nanotube based functional materials [31, 32]. We have shown that even small changes in diameter affect significantly the stiffness of SWNTs. This result implies that larger diameter SWNTs could yield stiffer fibers of low density, the density of SWNTs scales inversely with their diameter. Interestingly, recent experimental results show that large-diameter single and double-walled carbon nanotubes yield fibers with the best mechanical properties achieved so far [32, 33], although there are limitations, because excessively large few-walled carbon nanotubes are prone to buckle radially into flattened ribbons [34, 35].

Because stiffness is an important property in biological systems, the diameter-dependent rigidity of SWNTs should also be considered as potentially important variable in studies of interactions of carbon nanotubes with cells.

When only Brownian forces are present, we observe that relatively short SWNTs (below ~ 3 μm) behave as rigid rods in ambient fluid suspension and show translational and rotational diffusion but essentially no shape fluctuations [16, 36]. We find that the thermal shape fluctuations of longer SWNTs accurately follow the semiflexible filament model. Therefore, existing models for semiflexible networks should be applicable to the viscoelastic properties of concentrated SWNT suspensions [37], possibly by constructing model networks with tunable stiffness by using diameter-sorted SWNT samples [38]. In addition, the varying persistence lengths within the family of SWNT structures could be exploited to develop rod-like nano and microscale probes for microrheological studies of complex fluids and biological systems and to tailor

nanotube mobility in confined environments such as living cells and tissues [39]. [‡].

[‡]We will discuss this in the next chapter

Chapter 3

Orientational dynamics of SWNTs in a network

The motion of stiff objects in crowded environments has been investigated actively for more than three decades in polymer science and biophysics; yet, theory and experiments have not established whether slight flexibility affects the mobility of stiff slender filaments. Single-walled carbon nanotubes (SWNTs) are such thin filaments with tunable bending stiffness. We study the Brownian motion of individual SWNTs in agarose gel by infrared video microscopy. We find that SWNTs reptate in the network, and that their small flexibility enhances significantly their rotational in accord with Odijk's theory and in contrast with Doi's model of mobility of nearly rigid rods. This study establishes definitively the reptation dynamics of stiff threads and provides a framework to tailor SWNTs mobility in confined environments.

3.1 Introduction

Consider a tiny, slender filament (a snake, $\leftrightsquigarrow$), randomly wiggling through a maze. This was the "Eureka! "moment in polymer physics that yielded an intuitive approach to an almost intractable problem. In their seminal work, de Gennes, Edwards and Doi [40–42] modeled the effect of confinement on polymer dynamics by introducing the concept of preferential motion along the filaments axis, known as reptation. In this picture filaments snake through topological constraints of the surrounding network and their thermal undulations are confined to tube-like cages [40, 42].

Rod-like molecules are normally classified as flexible, semiflexible, or stiff depending on how effectively Brownian motion randomizes their shape. On a macroscopic level, reptation theory and virtual tube model have been successful in describing many collective properties of entangled polymer solutions and melts, in the limit of flexible ($L \gg L_p$) [43] and semiflexible ($L \sim L_p$) [44] polymers. At a single molecule level, the reptation motion of flexible polymers has been imaged directly by using fluorescently labeled DNA and is well established [2]. Reptation of semiflexible polymers has been imaged using fluorescently labeled actin as the model system, but only the confining tube been observed experimentally [45].

The limit of stiff polymers ($L < L_p$) , however, remains unexplored. Fundamental understanding of dynamics of confined stiff filaments is key to unlocking important questions in polymer dynamics, biophysics, and nanotechnology, e.g., the behavior of cell cytoskeleton and the motion of carbon nanotubes in cells and porous media.

Theoretically, the effect of confinement on dynamics of rod-like polymers was first described by Doi's cage model [46]. This model assumes that each rod is confined by collisions with a small number of surrounding rods and some small fixed number of confining rods is required to form a cage around a randomly chosen test rod. The average position for each of these confining rods passes with a distance of order of the cage diameter (ξ) from the center of the cage of test rod. Requiring that a fixed number of randomly distributed rods pierce a cylindrical cage of length L and diameter ξ yields a scaling relation:

$$\frac{\xi}{L} \sim \frac{1}{cL^3} \tag{3.1}$$

where c is the number density of rods. The cage is transient and has a lifetime of the

order of time:

$$\tau_{rep} \sim \frac{L^2}{D_{\parallel}} \tag{3.2}$$

required for the test rod to diffuse a length L ($D_{\parallel}$ is the longitudinal diffusivity).

According to Doi's model, longitudinal diffusion is unaffected by confinement and $D_{\parallel}$ retain its dilute value ($D_{\parallel}^0$) in dilute solution; however, the transverse diffusion is completely suppressed, $D_{\perp} = 0$. Considering slender-body hydrodynamics($D_{\parallel}/D_{\perp} \simeq 2$), the total self diffusion constant of a rod in confinement is given by:

$$D_s = \frac{1}{3}D_{\parallel} + \frac{2}{3}D_{\perp} \simeq \frac{1}{2}D_s^0 \tag{3.3}$$

where D_s^0 is the total self-diffusivity of a rigid rod in dilute solution.

To describe rotational diffusion, each rod is assumed to rotate a random angle of order $\delta\theta \sim \xi/L$ over the time $\tau_{rep} \sim L^2/D_{\parallel}$ required to escape its cage. This results in a rotational diffusivity:

$$D_r = \frac{(\Delta\theta)^2}{\tau} = \frac{k_B T}{\eta}\frac{\xi^2}{L^5} \tag{3.4}$$

It is clear that the mechanism of rotational diffusion of a rod in confinement relies upon longitudinal diffusion.

The motion of stiff filaments have been studied for many years. Bulk experiments such as birefringent techniques and depolarized dynamics light scattering of semiflexible rod-like polymers as well as simulations of rigid rods have been used to determine diffusion coefficients [47–49]. However, considerable deviations between both macroscopic experimental measurements, simulations and Doi's theoretical calculations have led to the need for modifications of the original theory by taking into account the effect of simplifying assumptions such as cage escape mechanisms [50,51], finite rod diameter [52] and rod flexibility effects [39].

Doi's model describes an entangled system of infinitely thin and not crossable rigid rods. However, excluded volume can effect the rod dynamics. Edwards and Evans [53] argued that when rotational diffusion becomes sufficiently reduced, the longitudinal motion of the rod can also be reduced due to collisions with the neighboring rods which in return further slows down the rotational diffusion.

Sato and Teramoto [54], introduced the concept of "fuzzy cylinder" to take into account both the effect of excluded volume as well as finite flexibility. In their model, any excluded volume interactions will cause a decrease in longitudinal diffusivity ($D_{\|}$) which in return causes an increase in the caging time and hence D_r. To take into account the effect of flexibility, they replaced the diameter of the rod by a larger effective diameter of a "fuzzy cylinder" of the order of the filaments equilibrium transverse thermal bending fluctuations ($L^{3/2}/L_p^{1/2}$) which according to their model will cause a decrease in longitudinal diffusivity and hence a decrease in D_r.

Odijk considered the effect of finite flexibility of rods on the predicted confinement of long, thin rodlike polymers. In Odijk's ansatz [39], the tubelike cages would only suppress the thermal undulations longer than a wavelength, λ ,namely deflection length. While the contour length, L , and the persistence length, L_p, describe the properties of the single polymer and the pore size, ξ , is the characteristic length scale of the confining network, Odijk's deflection length, λ , captures the interaction between both and is defined as (see figure 3.1):

$$\lambda = \left(L_p \xi^2\right)^{1/3} \tag{3.5}$$

Over the contour length range $\xi < L < \lambda < L_p$, the stiff filament behaves effectively as a rigid rod. The rotational diffusion coefficient is determined by reptation-rotation of the rod and decreases by decreasing the size of the cages, ξ, or by increasing the contour length of the rod. In this regime Doi's rigid rod theory is recovered.

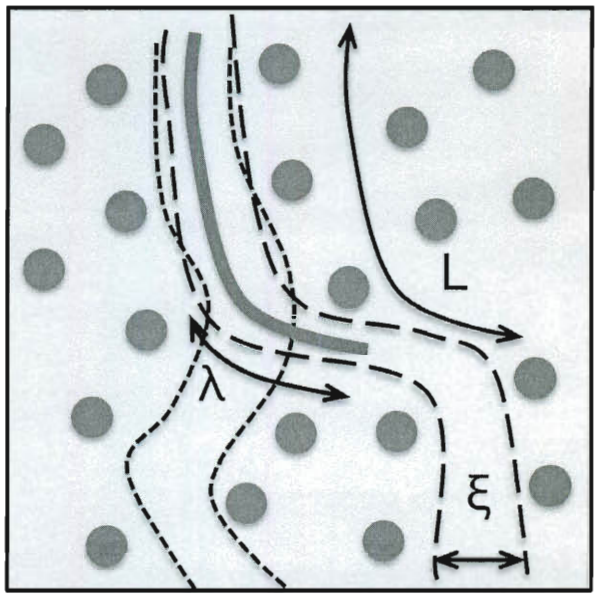

Figure 3.1 : Schematic of a stiff thread in a fixed network (L is the length of the thread, λ is the deflection length and ξ is the pore size of the network

However, the effect of flexibility is large when the filament's contour length lies in the range $\xi < \lambda < L < L_p$. The fingering of segments as large as the deflection length assists in tube remodeling and relieves the constraint on the rod's rotation with translation through its contour length. This leads to faster rotational diffusivities with considerably less length- and no pore size- dependence. In summary, by taking into account finite flexibility, for rotational diffusion of a rod in confinement two regimes exist (see figure 3.2):

$$D_r = \begin{cases} \frac{k_B T}{\eta} \frac{\xi^2}{L^5} & \xi < L < \lambda < L_p \\ \frac{k_B T}{\eta} \frac{1}{L^2 L_p} & \xi < \lambda < L < L_p \end{cases} \tag{3.6}$$

where η is the solvent viscosity. Clearly there is a remarkable difference in length and pore size dependence in the respective regions.

To summarize, Doi [46] predicted that rotational diffusion is independent of stiff-

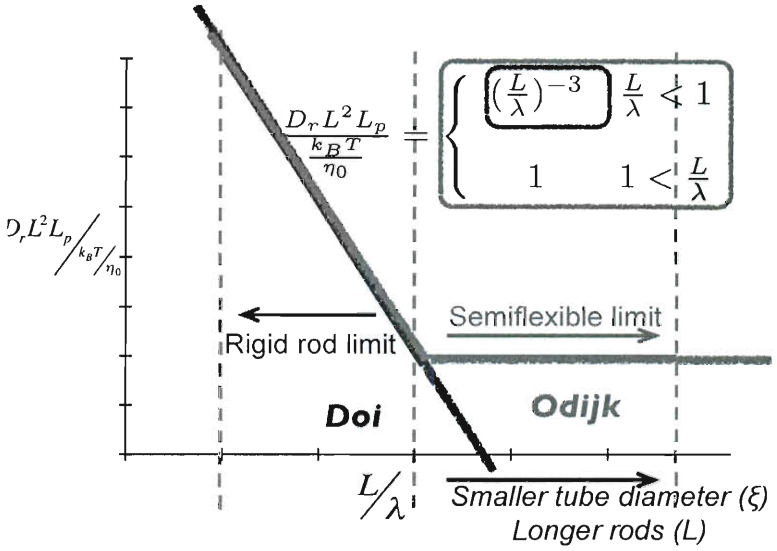

Figure 3.2 : Master plot comparing Doi and Odijk diffusivities

ness, while Odijk [39] concluded that such diffusion should be enhanced by flexibility and Sato [54] concluded the opposite. Macroscopic experiments that study the role of flexibility or finite diameter are sparse. Experiments on diffusion of short DNAs in polyacrylamide gels of different concentration have been successful in capturing Odijk's predicted scaling of rotational diffusion length dependence but failed to show the pore size independent diffusivities in this theory [55]. Also macroscopic measurements suffer from complicating effects due to polydispersity, aggregation, and attractive forces as well as strong coupling between translational and rotational diffusivities, which make the interpretation of the results very difficult.

At the single molecule level, the orientational dynamic behavior of stiff filaments, affected by chain flexibility, has never been reported or tested before. It represents a great challenge due to lack of a well-characterized optically anisotropic stiff filament

model system that can capture the $L < L_p$ regime.

SWNTs are high aspect ratio rolled sheets of graphene that can be classified as polymers [16, 56]. SWNTs have diameters of 0.7-1.2 nm, lengths of few microns and persistence lengths of about 20-100 μm depending on their diameter [57], yielding thermal fluctuations that can be observed by optical NIR fluorescence microscopy. As such they are experimentally ideal model systems for stiff polymers in the regime where $L < L_p$ and can address important open problems in polymer physics by bridging the gap between the theory and single molecule experiments.

Here, we show direct evidence of individual SWNTs reptating in a fixed network by near infrared fluorescence microscopy [6]. We verify that even slight flexibility in stiff filaments has a marked effect on orientational dynamics of the filament. We address some of the open questions:

- How does filament flexibility affect rotational diffusivity? Does rotational diffusivity increase with flexibilty as realized by Odijk, leading to a pore size independent rotational diffusion coefficient as well as a marked difference in rotational diffusion length dependence?

- How does filament flexibility affect the longitudinal diffusivity of stiff filaments?

We will also discuss other question whether the crossover between Doi's model and Odijk's model the signature of the crossover between loosely entangled and tightly entangled concentration regime?

3.2 Experiments

3.2.1 SWNTs

SWNTs with diameter between 0.7 and 1.2 nm were obtained from Rice University HiPco reactor (batches 162.8 and 189.2 without purification). Dilute ($\sim$ 1 ppm) aqueous suspensions of SWNTs in 1 wt% sodium deoxycholate surfactant (DOC, Sigma) were prepared by mild tip ultrasonication (7 W, 10 s, Microson, Misonix) to minimize SWNTs breaking.

3.2.2 Porous medium: Agarose gel characterization

Agarose gel structure

Polysaccharide gels occur in many biological systems. Gel formation is generally associated with transformation of disordered biopolymers to a partly ordered state, a change sometimes referred to as a random coil-to-helix transition. Agarose has an alternating backbone consisting predominantly of 3-linked β-D-galactopyranose and 4-linked 3,6-anhydro α-L-galactopyranose residues. It forms firm, slightly turbid gels on heating $>$ 0.2 wt % aqueous dispersions of the polymer to above 90°C and then cooling to about 30°C. Remelting requires temperatures in excess of 80°C, in other words, there is marked thermal hysteresis. On heating to above the helix-coil transition, the chains disorder, that is to say double helix melt. On recooling the individual chains partly revert to the native double helix forms and the sharing of helices between different polymer chains produces the physical cross-links. Each chain can share portions of ordered helical structure with at least two other chains-an essentially condition for branching and subsequent gel formation. [58]

Theory

Strong and weak gels can be classified based on their mechanical spectra. The typical strong gel spectrum, over the frequency range of 10^{-2} to 10^{2} rad/s, consists of two nearly horizontal straight lines. G' is typically 1-2 orders of magnitude greater than G''. Quite often the dynamic analysis of strong gels is restricted to the elastic component G' justified by the relative values of G' and G'. Strong gels behavior can be summarized as following: G' is always much greater than G'' and there is a slight frequency to zero dependence over a wide of frequencies. If this behavior is extended to zero frequency then the system will exhibit an equilibrium or static shear modulus, G_e, which is a characteristic of viscoelastic solid like networks. [58, 59]

Rubber Elasticity theory Invoking the theory of rubber elasticity, one considers a polymer chain in a crosslinked network as an entropic spring. When the chain is stretched, the entropy is reduced by a large margin because there are fewer conformations available. Therefore, there is a restoring force, which causes the polymer chain to return to its equilibrium or unstretched state, such as a high entropy random coil configuration, once the external force is removed. This is the reason why rubber bands return to their original state. [60]

The equilibrium stress-stretch behavior of elastomeric materials can be captured by statistical mechanics treatments of rubber elasticity. [60]

A common idealization of a lightly crosslinked rubber is a network of tetrafunctional connectivity in which four strands radiate from each crosslink; the strands are of equal length; dangling molecular ends are negligible; and the deformations are affine i.e. the crosslinks move in an affine manner. The classical rubber elasticity theory [59] specifies for this case that the equilibrium shear modulus in infinitesimal

deformations is given by:

$$G_e = g\frac{\overline{r_E^2}}{\overline{r_0^2}}\nu^* RT \tag{3.7}$$

where ν^* is the moles of network strand per cm^3 and g is a numerical factor close to 1. The ratio $\overline{r_E^2}/\overline{r_0^2}$, where $\overline{r_E^2}$ is the end-to-end distance of a strand and $\overline{r_0^2}$ is the mean square end-to-end distance which strand of the same length would assume if not constrained by cross-links, is assumed to be close to 1 at temperature and concentration the network was formed and at all temperatures. [61, 62]

Experiments

Rheological measurements completely describe the mechanical response of a material on a macroscopic scale. Complex, viscoelastic materials display properties of both solids and liquids and can be fully characterized by their frequency-dependent complex shear modulus. Large structures found in many complex materials have the ability to constrain small particles or macromolecules. At length scales where the constraining effects of these structures become important, the microscopic response is no longer connected to the bulk response by simple scaling laws, and direct local measurements are essential. A combination of local and bulk measurements can best describe the response of such complex materials. [63]

Sample preparation The agarose used in our experiments is MP, LM Agarose from Roche. The agarose powder is dissolved in DI water (0.5, 1, 2 % w/w) and heated up to about 90° C. Then the solution is cooled down to below 30 ° C. For rheology measurements, the gel is casted in Petri dish (the gel thickness acquired is about 1 mm) and then molded out in 25 mm or 40 mm diameter discs.

Instruments Rheological experiments are performed using AR2000 (Stress-controlled rheometer) and ARES (Strain-controlled rheometer), equipped with parallel-plate ge-

ometry (25 mm-diameter upper stainless steel plate for AR2000 and 40 mm-diameter upper and lower plate for ARES). Samples are allowed to thermally equilibrate for several minutes after loading, and a solvent trap, saturated with DI water, is used to minimize evaporation during the course of each experiment.

Measurements: Linear viscoelastic characterization

- **Dynamic Strain Sweep Test** In order to find the critical strain for linear viscoelasticity, elastic and loss moduli ($G^{'}$ and $G^{''}$) are measured against oscillatory strain deformation from 0.1 to 50 at three different radial frequencies (0.1, 1 and 10 rad/s). Figure 3.3 shows the log-log plot of elastic modulus as a function of strain for a sample of 0.5 wt % agarose concentration at three different frequencies (0.1, 1 and 10 rad/s). From it is evident the data the linear viscoelastic strain extends to 0.15 (0.2).

- **Dynamic Frequency Sweep Test** Using the strain value from linear viscoelastic region established from dynamic strain sweep test, $G^{'}$ and $G^{''}$ are measured from ω=100 to 0.01 rad/s. For each gel concentration the experiments are performed first at low number of points per decade and then large number of points per decade to rule out any aging phenomena during measurements. This gives the mechanical spectrum of the gel (the log-log plot of $G^{'}$ and $G^{''}$ vs. ω). Figure 3.4 shows the mechanical spectra of different concentrations of agarose using ARES (3.4(a)) and AR2000 (3.4(b)) rheometers. For strong gels such as agarose, $G^{'} > G^{''}$ (not shown) and both moduli are largely independent of frequency. As evident by the plots this behavior extends to very low frequencies. By extrapolating the data from the frequency dependent of the elastic modulus to very low frequencies, we can obtain the equilibrium elastic

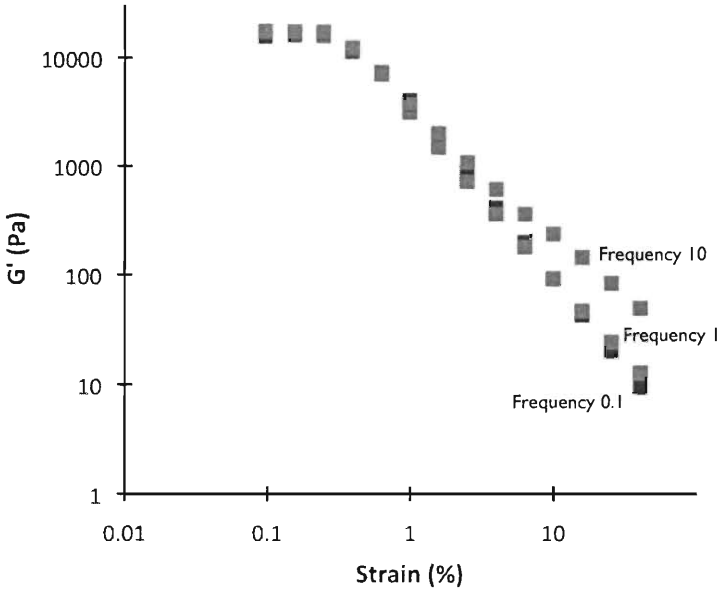

Figure 3.3 : strain sweep test (agarose 1 % w/w)

modulus (G_e) for the gels. The concentration dependence of this modulus takes a characteristic form that will be discussed later.

Results

Analysis of concentration effects on plateau elastic modulus Plateau elastic modulus can be obtained from dynamic data (as described) in order to determine its concentration dependence. Strong gels can be easily investigated since G' is almost frequency independent and can be therefore approximated to the plateau or equilibrium elastic modulus [59]. For physical gels, the rubber elasticity theory predicts that G_e is proportional to c^2 [59]. Figure 3.5 shows the concentration dependence of G_e, which is proportional to $c^{2.2}$. The difference in the exponent (2.2 vs. 2) can be explained as follows: biophysical gels differ from physical gels in the sense that

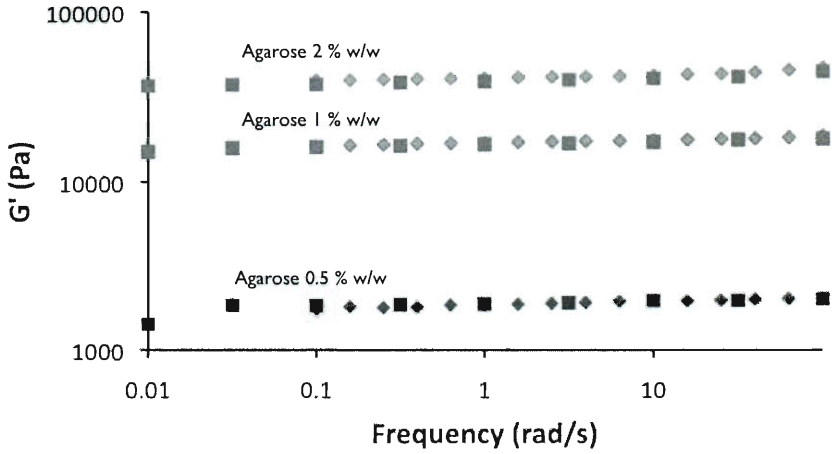

(a) Ares Rheometer (at 0.15 % strain)

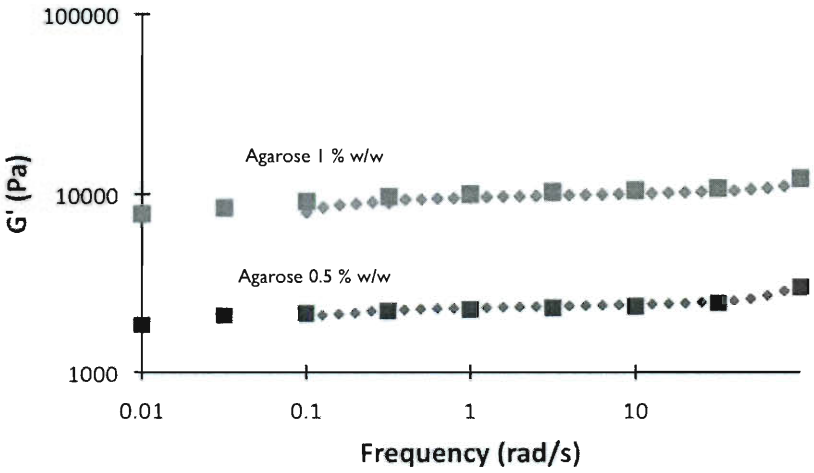

(b) AR2000 Rheometer (at 0.2 % strain)

Figure 3.4 : Frequency Sweep Test

formation of biogels such as agarose gel is associated with the formation of extended junction zones rather than point covalent crosslinks and these extended junctions are somewhat transient in nature. Thus there is equilibrium between the making and breaking of junctions with certain degree of reversibility. de Gennes [64, 65] has predicted a limiting behavior $G_e \propto c^{2.25}$ by noting the parallel between the osmotic pressure of semidilute polymer solutions and the modulus of gels. This relationship fits our data better which could be interpreted as an extra contribution from the presence of network defects such as trapped entanglements or lateral association of multiple helices and the dynamic nature of the crosslinks.

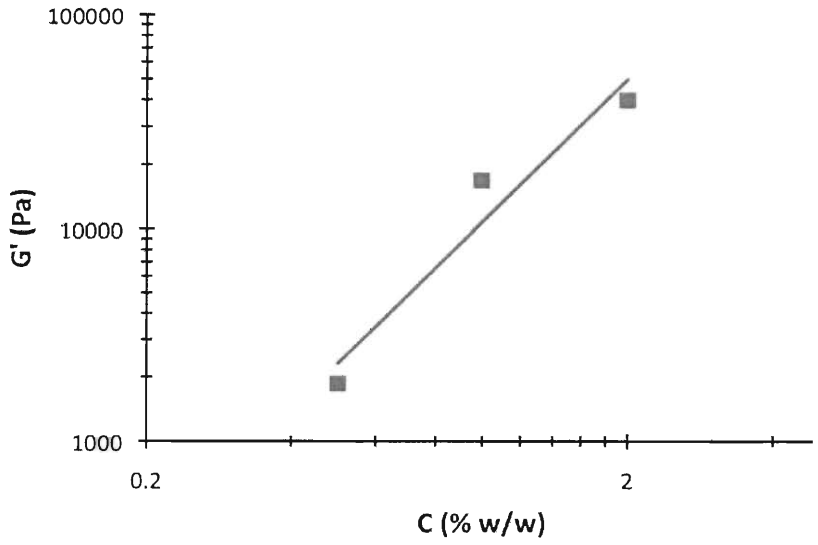

Figure 3.5 : Concentration dependence of plateau elastic modulus

Gel pore size as a function of concentration Knowing the equilibrium elastic modulus of gels, an effective gel pore size can be calculated from rubber elasticity

theory [59, 60]:

$$G_e = \frac{g\nu RT}{N_A} \tag{3.8}$$

where ν is the number concentration of crosslinks and N_A is the Avogadro's number. The effective pore size ξ is given by $\nu^{-1/3}$:

$$\xi = \left(\frac{G_e N_A}{RT}\right)^{-1/3} \tag{3.9}$$

All pore size values calculated from rubber elasticity theory are plotted as a function of the gel concentration in figure 3.6 We find power law dependence of $\xi \propto c^{-\gamma}$ where γ is 0.74, in excellent agreement with the value predicted by de Gennes [66] for a network of flexible chains from scaling arguments, $\gamma = 3/4$.

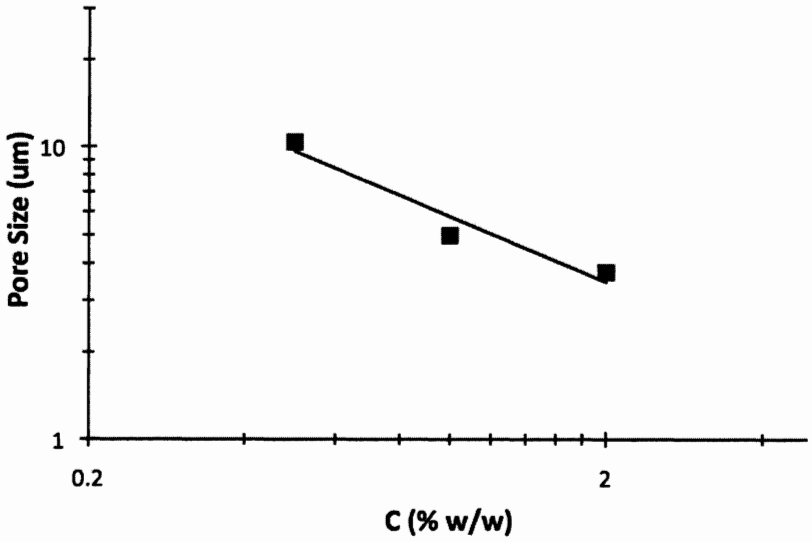

Figure 3.6 : Concentration dependence of pore sizes

However, We measure the pore sizes to be very small. This indicates that while agarose does contain large elastic structures that span the sample and bear stress

macroscopically, at short length scales, these structures do not form a homogeneous elastic continuum; instead, agarose is characterized by many smaller voids, or pores through which smaller particles may move. [63]

Conclusion

With rheological measurements we have characterized concentration dependence of equilibrium elastic modulus and pore sizes of agarose gel. From the relationship between pore size and elastic modulus given by rubber elasticity theory, $\xi \propto (G_e)^{-1/3}$, we determined the pore size dependence for different concentration of the gels as $\xi \propto c^{-0.74}$, in agreement with the value predicted by de Gennes for a network of flexible chains from scaling arguments. In agarose, large fibrous polymers form heterogeneous elastic structures that bear macroscopic stress but allow the motion of particles in confined pores. It has been shown previously [63] that despite the significant differences between macroscopic rheological properties and the microscopic environment explored by small particles, the variation within local microenvironments is quite small, of order 20%. In our pore size measurements we have scaled our pore sizes accordingly so even if the value of pore sizes are not accurate, the scaling is the same.

3.2.3 Microscopy samples

Agarose

Purified agarose (Multi Purpose, Roche) was used without further purification. Agarose gels were prepared by adding the 1 mL of DOC surfactant solution (1 wt %, pH = 7.0) to 0.05 g of agarose powder (5 wt % agarose gel concentration) in a sealed glass vial; the vial was then heated to about 90°C in a water bath until complete dissolu-

tion of the polymer. Solutions were covered and kept at 80°C at above gelation point for further steps. If necessary drops of hot water were added to keep the polymer fraction constant.

In a typical experiment, a few μL of SWNT solution were added to few 100 μL hot clear solution of agarose and were mixed together very well using vortex mixer to get the final agarose concentration of 0.5-2.5 wt%.

5-10μL of the solution was sandwiched between a heated #1.5 coverslip and microscope slide. The cell was sealed using vacuum grease and cooled to room temperature (which is below the gelling temperature of 37°C) and thus triggering the gelation of the agarose. It is important to note that SWNT/DOC does not interact with agarose gel [67].

Experimental setup

Nanotubes were excited by either a frequency doubled YAG laser, a tunable dye laser (rhodamine) or a tunable Ti:Sa laser depending on the chirality of the SWNTs to be resonantly excited at their second order transition(cite). The beams were focused into the back aperture of a high NA objective (100x or 60x, Numerical Aperture 1.4), with excitation intensities between 0.1-10 kWcm^2 of circularly polarized light. The fluorescence was collected with the same objective and imaged on a low noise Si-CCD camera (Micromax, Roper Scientific) or NIR InGaAs camera (Xenics) depending on the chirality of the nanotubes under study, to produce wide-field images of individual nanotubes. The emission spectrum of SWNTs was collected by a cryogenically cooled 1D InGaAs detector (OMA V, Roper Scientific) placed at the output of a spectrometer; We confirmed that at these irradiation levels there were no noticeable effects on the SWNT dynamics [68]. Images of SWNT dynamics were recorded at 30 frames

per second.

Image analysis

From the image analysis we obtained data sets consisting of SWNTs center of mass position in the lab frame and its orientation angle relative to the x-axis.

Orientation The overall shape of the SWNT was analyzed by enveloping its trace by a best fit ellipse that encompassed the shape of the SWNT and computed the lengths of the major and minor axes as well as the orientation of the resulting ellipse (figure 3.7).

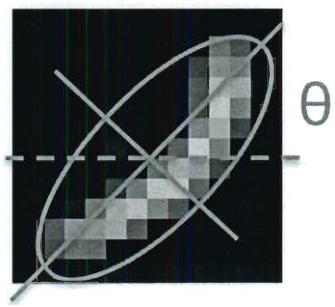

Figure 3.7 : Representative image of a SWNT in x-y lab frame, the orientation angle, θ, is the angle between the x-axis and the major axis of the best fitted ellipse to the shape of the SWNT

Center of mass position The center of mass position of SWNT in each frame is determined by weighting each pixel by its absolute gray level intensity, $r_i = [x_i, y_i]$, where i represents frame number spaced by 30 ms acquisition time. In this method the brighter pixels indicate a greater amount of SWNTs and give weight to where SWNT mass exist. This method could introduce error for the case of highly curved

backbones because the centroid can be located off the filament and any off-filament centroid would introduce error in mean square displacement data analysis in which the assumption is that the centroid is a point on the SWNT. However, because nanotubes are stiff and $L < L_p$ and relatively short, measuring the centroid through this method is sufficient and we verified the accuracy of the method for our images (figure 3.8) [69]. For experimental conditions where filaments are long, an alternate method should be employed where the filament center rather than its centroid is chosen.

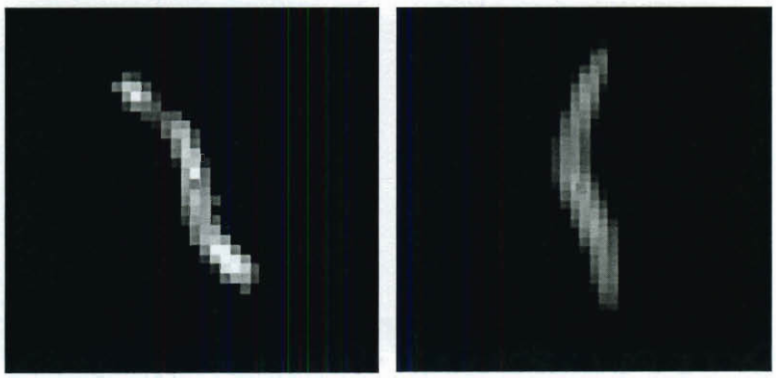

Figure 3.8 : Two images of a long SWNT is shown. The centroid position is on the filament

The displacements of the center of mass (MSD) or angle (MSAD) can be specified by a time averaged autocorrelation function given by (X is either angle (MSAD) or cartesian coordinates (MSD)):

$$MSD(MSAD) = \left\langle \Delta X^2(\tau) \right\rangle = \left\langle (X(t+\tau) - X(t))^2 \right\rangle \tag{3.10}$$

where τ corresponds to various lag times.

For the case of translational motion, the center of mass displacements were decomposed into its components parallel (Δn^2) and perpendicular (Δs^2) to the running time-averaged reptation tube:

$$\Theta_\tau = \langle \theta(t) \rangle_\tau = \frac{1}{\tau} \int_t^{t+\tau} \theta\left(t'\right) dt' \tag{3.11}$$

and applying the rotation matrix $R_{\Theta_\tau} = \begin{pmatrix} \cos\Theta_\tau & \sin\Theta_\tau \\ -\sin\Theta_\tau & \cos\Theta_\tau \end{pmatrix}$ to the cartesian displacements ($\Delta\hat{r}(t,\tau) = (\Delta s(t,\tau), \Delta n(t,\tau))$):

$$\Delta\hat{r}(t,\tau) = R_{\Theta_\tau} \Delta r(t,\tau) \tag{3.12}$$

and computing the time-average:

$$\Delta\hat{r}(\tau) = \frac{1}{\tau} \int_0^\tau dt \left[\Delta\hat{r}(t,\tau)\right] \tag{3.13}$$

The mean-square displacement at time lag $\tau = 0$ has a small non zero intercept due to tracking errors. Thus we can estimate the spatial and angular resolutions from intercepts of their corresponding MSDs [70]. Using this procedure we assign an orientation resolution of 2-5 ° and the spatial resolution of 40 nm along SWNT's short axis and 70 nm along SWNTs long axis due to superimposed tumbling motion [71].

3.3 Result and discussion

3.3.1 Reptation

We image directly the quasi-two-dimensional dynamics of SWNTs in agarose gel [72], a permanent network with pores $\sim$ 0.1-1 μm (depending on agarose concentration [73]), which mimics ideally the reptation ansatz of a thread moving in a fixed network of frozen obstacles.

The persistence length of each SWNT was determined from the emission spectrum of the individual nanotubes [57]. By image analysis, we extracted frame-by-frame each SWNT's center-of-mass position $r_i = (x_i, y_i)$ in the lab coordinates and its orientation relative to the x-axis. Figure 3.9 represent the center-of-mass trajectory of a 4.5 μm-long SWNT, in a 1.5% w/w agarose gel ($\xi \sim 0.2\mu m$) showing unequivocally snake-like motion. From the emission spectrum we identify the SWNT a (6,5) nanotube which

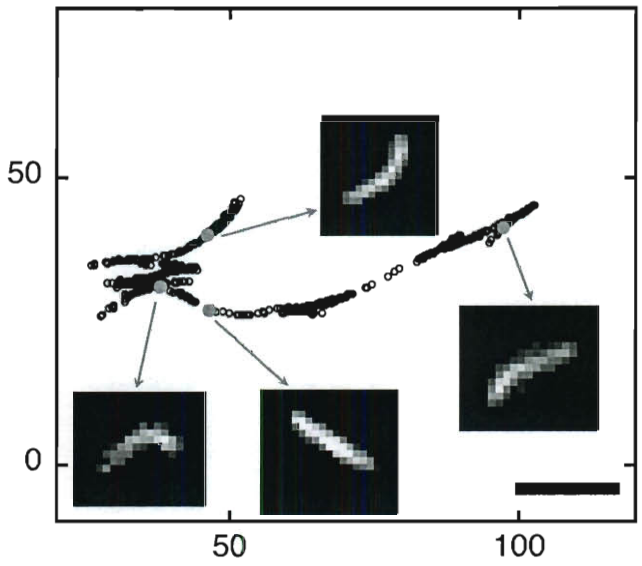

Figure 3.9 : Center of mass trajectories of a SWNT reptating in 1.5 w/w % agarose gel and representative near-infrared images of the SWNT illustrating the effect of flexibility on reorientation of SWNT in different pores (scale bar 5 μ m)

provides $d = 0.7$ nm and $L_p = 26$ μm [5, 57].

NIR fluorescence snapshots (see figure 3.9) clearly demonstrate that flexibility affects significantly reorientation of the SWNT in a new confining tube: at first the SWNT slides back and forth partially out of the confining tube; by bending slightly, the end of the SWNT has more freedom to explore various paths while translating

along its length, even though most of the SWNT is still caged and thus restricted to a certain orientation. Eventually, the SWNT completely slides out of the original confining tube and reorients in another tube.

3.3.2 Rotational diffusion

We quantify rotational motion by the statistics of the angle, θ_i. Figure 3.10 shows a

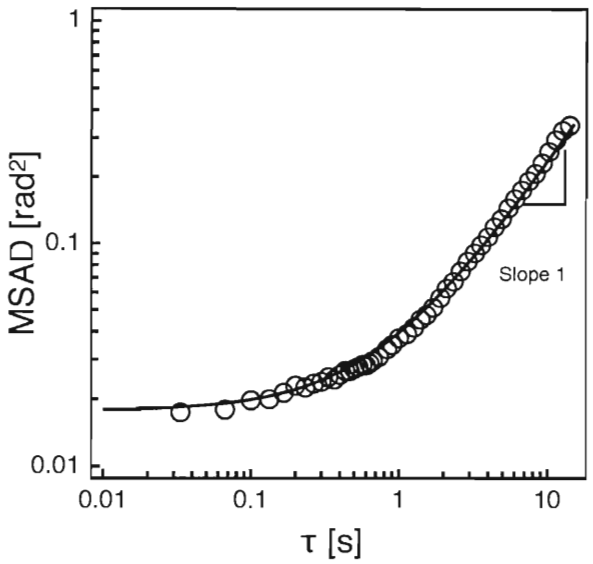

Figure 3.10 : Time evolution of angular MSD, shows the subdiffusive to diffusive behavior which occurs at disengagement time, τ_d. Line is the best fit to the data. D_r is calculated from the long time (diffusive behavior)

typical time evolution of mean-square angular displacement (MSAD), $\langle \Delta\theta^2 \rangle$. At short times, the SWNT's angular diffusion is sub-diffusive ($\langle \Delta\theta^2 \rangle \propto \tau^n$, n $\ll 1$), reflecting the confinement in the initial tube. At longer times, the SWNT diffuses out of the initial tube and the mean angular displacement behaves diffusively, $\langle \Delta\theta^2 \rangle = 2D_r\tau$, yielding the value of the rotational diffusivity, D_r. (Figure 3.11 shows all the SWNT

MSAD data vs. lag time.)

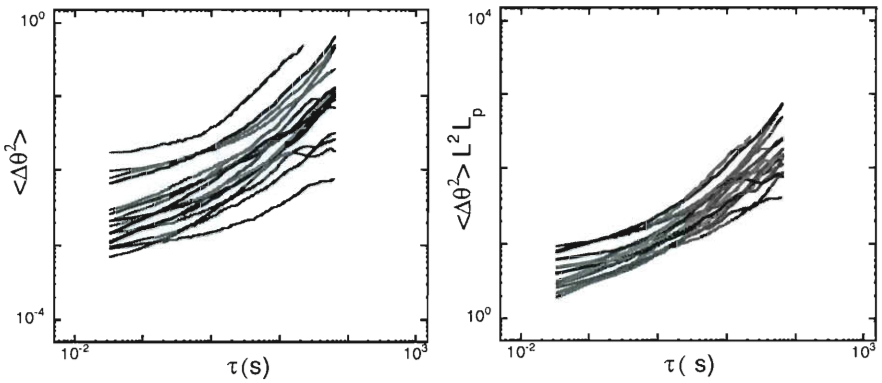

Figure 3.11 : Collapse of all MSAD vs. time curves by normalizing with respect to Odijk's rotational diffusivity

We measured the rotational diffusivity of 35 SWNTs with different lengths ($L \sim 2$ - 10 μm) and persistence lengths ($L_p \sim 26$ - 60 μm) reptating in agarose gels of several concentrations (hence pore sizes). We collapsed the rotational diffusivity on a master curve, by plotting the normalized rotational diffusivities $D_r/D_r^{Odijk} = D_r \eta L^2 L_p / k_B T$ versus normalized length L/λ. In such a plot (see figure 3.12), Doi's theory predicts a power-law with scaling exponent -3 ($(L/\lambda)^{-3}$) across the whole range of normalized length (dashed line in figure 3.12), whereas Odijk's theory predicts a plateau at ~ 1 for $L > \lambda$ (solid line in figure 3.12). The data show conclusively that, when $L \leq \lambda$, flexibility does not affect mobility (in agreement with both Doi and Odijk), whereas for $L > \lambda$, flexibility clearly speeds up long-time diffusion, which follows Odijk's scaling. In fact when we used Doi's rotational diffusivity for rescaling, the data did not collapse on a master curve (figure 3.13).

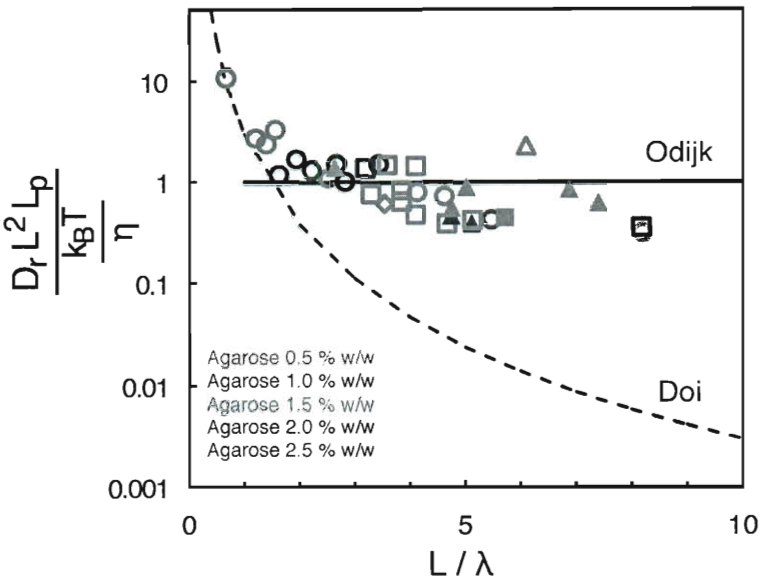

Figure 3.12 : Normalized rotational diffusivity of 35 SWNTs with different length and persistence length (denoted by different symbols) reptating in different concentrations of agarose gel versus normalized length by deflection length. Doi's theory is shown by a dashed line and predicts a power-law with scaling exponent -3 across the whole range of normalized length. Odijk's theory is denoted by a solid predicts a plateau at ~ 1 for $L > \lambda$

By plotting the rotational diffusivities versus length, we can back out the persistence length for each chirality set of nanotubes ($D_r \propto \frac{1}{L_p} L^{-2}$). The persistence length data agrees well with our previous measurements of L_p (figure 3.14) [57].

We now turn to the short-time sub-diffusive dynamics of the MSAD (figure 3.10). To cross over from short time sub-diffusive behavior to long time diffusive motion, a SWNT must diffuse by a length λ out of its initial confining tube. This occurs on a timescale known as the disengagement time, τ_d, which is the timescale a SWNT needs to reptate a length similar to deflection length and is determined from the free

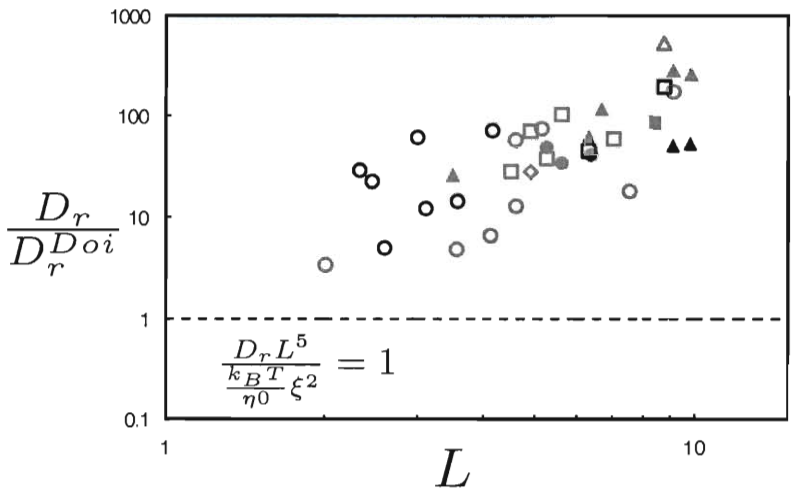

Figure 3.13 : Rotational diffusivities do not collapse with Doi's scaling: Doi's theory can not capture the dynamics of the system

parallel diffusion constant of the center of the mass [39]:

$$\tau_d = \frac{\lambda^2}{D_\perp} \sim \frac{\eta \lambda^2 L}{k_B T} \tag{3.14}$$

At times shorter than τ_d, the SWNT wiggles freely inside its initial confining tube, with minimal angular reorientation ($\tau < \xi/L$, hence the sub-diffusive behavior of MSAD in 3.10). At times longer than τ_d, the SWNT slides out of the initial confining tube and starts exploring the other accessible tubes. Figure 3.15 shows the disengagement times normalized to λ^2 for 11 SWNTs by fitting the MSAD with $\langle \Delta\theta^2 \rangle = \theta_0^2 + 2D_r\tau$ and setting $\tau_d = \theta_0^2/2D_r$. We find that the measured τ_d normalized by deflection length λ^2 scales linearly with length L, confirming Odijk's prediction for short-time translational diffusion.

We note here that these 11 nanotubes were imaged by a 100x objective and hence

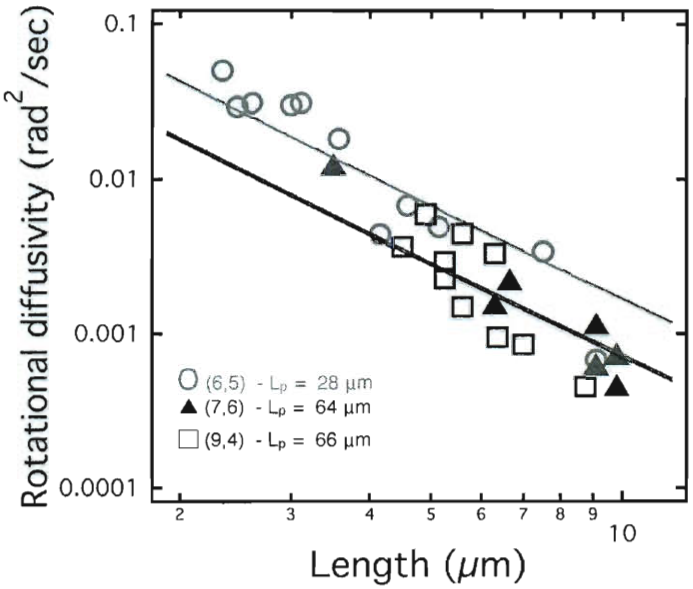

Figure 3.14 : Persistence length of three chirality nanotubes determined from rotational diffusivity data

smaller pixel size. We could not observe the expected behavior of τ_d for lower magnification objective (60x). The errors introduced by the limited angular resolution in our measurements can affect the interpretation of the short time dynamics. The microscope angular resolution is a/L where a is the pixel size. Therefore, resolution limits our experiments below a resolution time of $\tau_{resolution} \cong a^2 L_p \pi\eta/2k_BT$. In the experimental conditions of figure 3.15, $\tau_{resolution}/\tau_d = \left((\lambda/L)\,(a/\xi)^2\right)/4$ ranges from 0.01 to 0.26; therefore, $\tau_r >> \tau_d$ and resolution does not affect significantly the measurement of the subdiffusive regime due to the short-time dynamics in the system.

One important issue that needs to be addressed here is the effect of pore size heterogeneity on our measurements. Agarose large fibrous polymers form heterogeneous

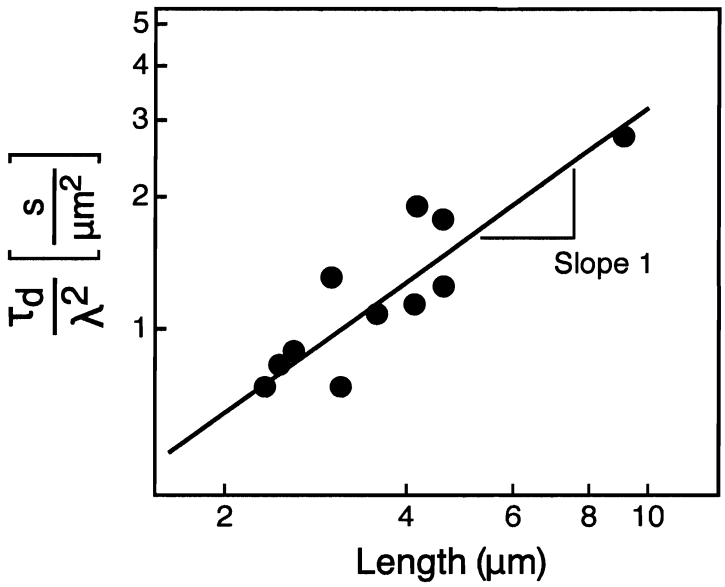

Figure 3.15 : The disengagement time normalized by deflection length (λ^2) scales linearly with length L.

elastic structures that withheld macroscopic stress but allow the motion of particles in confined pores. The polydispersity in pore size has been estimated to be of order 20% . The theories of Odijk and Doi assume a distribution of pore sizes with a characteristic pore size, ξ [63]. A SWNT explores different static microenvironments over the course of the measurement, resulting in a time-averaged characteristic pore size that is not a representation of any instantaneous microenvironments. Because we follow each SWNT for $\tau_r >> \tau_d$, each SWNT explores many pores (of the order of $\frac{\tau_r}{\tau_d} \propto \left(\frac{L}{\lambda}\right)^2 \frac{L_p}{L} \geq 25$ and each SWNT samples a reasonable pore distribution.

The rotational dynamic behavior of SWNTs in a fixed network can be a starting point to study the dynamics of concentrated solutions of SWNTs as well as SWNT composite materials. A concentration independent value for D_r would be consistent with theoretical predictions for tightly entangled solutions [74, 75]. As the concen-

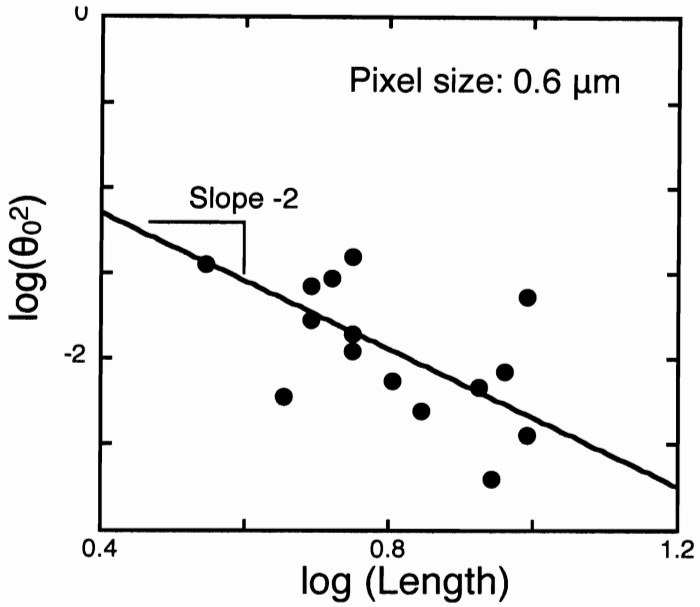

Figure 3.16 : MSAD short time subdiffusivity due to limited resolution

tration of a solution of semiflexible filaments is increased, the cage radius defined by equation 3.1 decreases. Above a crossover concentration c^* the cage diameter (ξ) predicted for a solution of rigid rods drops below the equilibrium transverse amplitude fluctuations of a semiflexible filament, $L^{3/2}/L_p^{1/2}$. Beyond this concentration both rotations and bending fluctuations of molecules are hindered by neighboring filaments and hence creating a tightly entangled solution. Now we have the same picture as reptation of a stiff filament in a fixed network: reptation along a slightly curved tube causes a change in the end-to-end orientation of order $\langle \delta\theta \rangle \sim (L/L_p)^{0.5}$ per reptation time [74]. This predicted D_r depends upon concentration to the extent that $D_{||}$ depends on concentration which is very different from the strong concentration dependence $D_r \sim c^{-2}$ predicted for entangled rigid rods and loosely entangled semiflexible rods [74]. So one can argue that the signature of the crossover between

loosely entangled and tightly entangled concentration regime is a saturation of D_r to a nearly concentration independent value.

3.3.3 Translational diffusion

In order to understand the the dynamic of the system on time scales less than the rotational diffusion time we looked at the translational diffusion. Because SWNTs explore orientation space by reptating in and out of pores, rotational and translational diffusion should be strongly coupled at time scales below the rotational diffusion time. Such coupling occurs even in the much simpler case of two-dimensional Brownian motion of an unconstrained ellipsoid, and is well described in terms of Perrin-Smoluchowski theory [71]. Theoretical calculations and simulations have recently shown that this same theory can capture such coupling in the motion of confined rigid filaments (infinite L_p) [49]. To investigate this coupling experimentally we measured the evolution of center-of-mass mean square displacements (MSDs) parallel Δs^2 and perpendicular Δn^2 to the time-averaged orientation of the reptation tube.

Figure 3.18 shows the decomposed parallel and perpendicular MSDs versus time (normalized by the rotational diffusion time). In order to investigate the spectrum of timescales arise in the system at short times less than rotational relaxation we will first look at the dynamics of a point along the SWNT backbone that is undergoing Brownian motion. The dynamics of this point is governed by continuum elastic bending modes of the SWNT. The x-axis represents the average orientation of the SWNT. The SWNT will have small transverse undulations where $u(x,\tau)$ and $v(x,\tau)$ are the two independent transverse degrees of freedom (see figure 3.17):

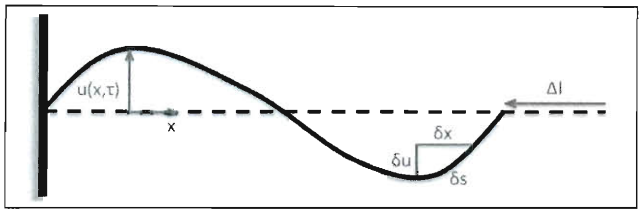

Figure 3.17 : Schematic of a motion of an elastic filament

The tangent angle ($\theta \approx \frac{\delta u}{\delta x}$) can be decomposed into a series of Fourier cosines:

$$\theta(s) = \sqrt{\frac{2}{L}} \sum_q a_q cos(qs) \tag{3.15}$$

where $q = \frac{n\pi}{L}$ is the wavevector. In terms of u:

$$u(x,\tau) = \sqrt{\frac{2}{L}} \sum_q u_q sin(qx) \tag{3.16}$$

where $a_q = qu_q$.

The bending energy can be written as [26]:

$$U = \frac{\kappa}{2} \sum_q q^2 a_q^2 \Rightarrow U = \frac{\kappa}{2} \sum_q q^4 u_q^2 \tag{3.17}$$

According to equipartition of energy each quadratic term in equation 3.17 (each excited mode) contributes $\frac{1}{2}k_BT$ to the total energy [26]:

$$\frac{1}{2}k_BT = \frac{\kappa}{2}q^4 u_q^2 \Rightarrow \frac{k_BT}{\kappa q^4} = u_q^2 \tag{3.18}$$

The MSD of a point at distance x along the baseline of the filament is (note that the dynamical behavior from autocorrelation of the fluctuating bending modes

$\langle u_q(t)\, u_0(t)\rangle$ is approximated by a single exponential [19]):

$$\left\langle \Delta u^2(x,\tau)\right\rangle = \left\langle [u(x,\tau) - u(x,0)]^2\right\rangle \tag{3.19}$$

$$\Rightarrow \left\langle \Delta u^2(x,\tau)\right\rangle = \frac{2}{L}\sum_q u_q^2 \sin^2(qx)\left(1 - e^{-\omega(q)\tau}\right) \tag{3.20}$$

$$\Rightarrow \left\langle \Delta u^2(x,\tau)\right\rangle = \frac{2}{L}\sum_q \frac{k_B T}{\kappa q^4} \sin^2(qx)\left(1 - e^{-\omega(q)\tau}\right) \tag{3.21}$$

Due to the viscous interaction with the solvent, each mode has a different characteristic decay time according to its wave number given by [26, 76]:

$$\tau_q = \omega(q)^{-1} = \frac{\zeta}{\kappa q^4} \tag{3.22}$$

The undulation amplitude at a single point results from the summation of contributions from individual bending modes with energy density κq^4, each one driven by thermal energy $k_B T$ (3.21).

For a given time, τ, those modes with relaxation times (τ_q) faster that τ ($\tau_q < \tau$) will contribute to the MSD of undulations. The relaxation time corresponding to the longest wavelength mode sets an important cutoff, below which we can expect saturation of the undulation amplitude.

At short times the number of contributing modes grows with time, from the shortest toward the longer wavelength [76, 77]. Thus the response of the filament is more local the shorter the time interval on which its motion has been observed. To realize the time dependence of equation (3.21), we consider terms that have units and carry out the sum up to a time dependent long wavelength cutoff where $\tau = \omega(q_*)^{-1}$ thus $q_* \sim (\kappa\tau)^{-\frac{1}{4}}$:

$$\left\langle \Delta u^2(x,\tau)\right\rangle \sim \frac{1}{L}\sum_{q_*}^{\frac{\pi}{d}} \frac{k_B T}{\kappa q^4} \sim \int_{q_*}^{\frac{\pi}{d}} dq \frac{k_B T}{\kappa q^4} \sim \frac{k_B T}{\kappa q_*^3} \sim \frac{k_B T}{\kappa^{\frac{1}{4}}} \tau^{\frac{3}{4}} \tag{3.23}$$

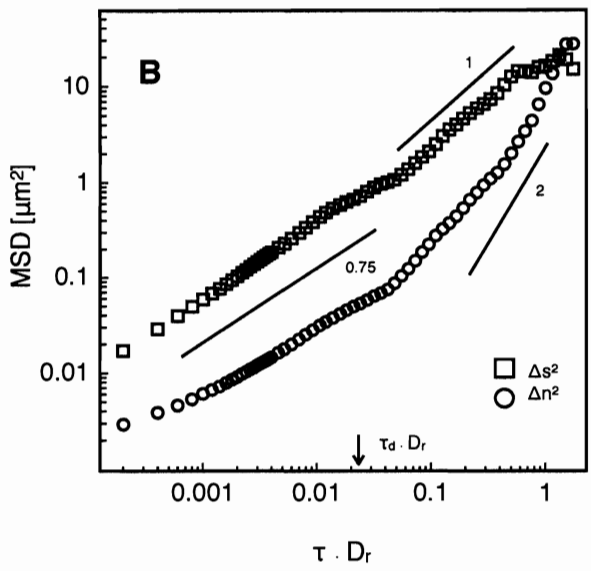

Figure 3.18 : Short time reptation dynamics: $\tau < \tau_d$ is the dynamics inside the tube, $\tau_d < \tau < \tau_r$ is the crossover region between anisotropic and isotropic diffusion and $\tau > \tau_r$ is the isotropic diffusive long time dynamics

Now we look at the behavior we observe in figure (3.18) for transverse MSD (Δn^2) in the case of reptation dynamics of SWNTs in a network: At short times ($\tau < \tau_d$), SWNT diffusion is clearly anisotropic i.e., $\Delta s^2 \gg \Delta n^2$; SWNTs diffuse much faster parallel than perpendicular to the tube axis. In this time regime, the dynamics of center-of-mass is dominated by the relaxation of thermally excited elastic bending modes of the SWNT, with relaxation times $\tau_r^n \sim \eta l_n^4/\kappa$, where l_n is the mode wavelength. For a given time τ, long-wave modes ($\tau_r^n > \tau$) are effectively *frozen*, whereas short-wave ones (τ_r^n) evolve and contribute to the amplitude of thermal undulations. At time τ , the longest (dominant) bending mode has a wavelength of $l(\tau) \sim (\kappa\tau/\eta)^{\frac{1}{4}}$. The mean square amplitude transverse fluctuations (Δu^2) of this mode dominate the transverse diffusion of the center of mass, and evolves with time

as [26, 76, 77]:

$$\Delta u^2 \approx \Delta n^2 \sim \frac{l(\tau)^3}{L_p} \tau^{\frac{3}{4}} \tag{3.24}$$

which is indeed the sub-diffusive power law $\tau^{\frac{3}{4}}$ we measure (figure 3.18). The same time dependence is also expected for the mean square amplitude of the longitudinal fluctuations of the SWNT [26, 77]; Note that for long times, all modes are saturated and the MSD reaches a constant amplitude:

$$\left\langle \Delta u^2(x,\tau) \right\rangle \sim \int_{\frac{\pi}{L}}^{\frac{\pi}{d}} dq \frac{k_B T}{\kappa q^4} \sim \frac{k_B T}{\kappa} L^3 \sim \frac{L^3}{L_p} \tag{3.25}$$

where for the case of reptation, due to confined motion of SWNT in a tube with diameter ξ, the longest wavelength that relaxes is λ, before SWNT disengages from the first confining tube and slides into another tube:

$$\left\langle \Delta u^2(x,\tau) \right\rangle \sim \xi^2 \sim \frac{\lambda^3}{L_p} \tag{3.26}$$

So we can see that λ or deflection length is the longest wavelength that has not been suppressed [39].

We should note here that besides thermal bending fluctuations another contributing factor to the dynamics of short times, is the perpendicular and parralel diffusive motion. For the case of perpendicular motion ($\delta u_\perp^2(\tau)$):

$$\left\langle \Delta u^2(x,\tau) \right\rangle \sim \frac{k_B T}{\kappa^{\frac{1}{4}}} \tau^{\frac{3}{4}} + \delta u_\perp^2(\tau) \tag{3.27}$$

$$\left\langle \Delta u^2(x,\tau) \right\rangle \sim \frac{k_B T}{\kappa^{\frac{1}{4}}} \tau^{\frac{3}{4}} + D_{\perp 0} \tau \tag{3.28}$$

$$\left\langle \Delta u^2(x,\tau) \right\rangle \sim \frac{k_B T}{\kappa^{\frac{1}{4}}} \tau^{\frac{3}{4}} + \frac{k_B T}{L} \tau \tag{3.29}$$

The value of the second term saturates at a timescale called entanglement time, τ_e:

$$\tau_e = \frac{\xi^2}{D_{\perp 0}} \tag{3.30}$$

In our experiments τ_e is smaller than τ_d so in the regime where $\tau_e < \tau < \tau_d$ the time dependence arises due to thermal bending fluctuations of the filament rather the translational diffusion. In fact for the case of a rigid rod [78], in this regime, one observes a plateau of $\langle \Delta u^2(x,\tau) \rangle$.

Now we look at the long time dynamics: at longer times, Δs^2 crosses over to a linear diffusion regime, indicating that the SWNT has fully reptated along its length ($\Delta s^2 \sim \tau$). In this crossover regime, the transverse MSD Δn^2 grows super-linearly with time because reptation occurs along a curved path [78,79], a motion that couples rotation and translation ($\Delta n^2 \sim D_\perp \tau \cdot \Delta\Theta^2 \sim \tau^2$). At times longer than rotational diffusion time, the SWNT loses memory of its initial orientation, and its diffusion becomes isotropic.

Figure 3.19 shows $\Delta n^2/\Delta s^2$ for all the SWNTs. The data shows clearly the anisotropic diffusion that is significantly increased with increasing the confinement.

On intermediate timescales between disengagement and rotational diffusion times ($\tau_d < \tau < \tau_r$), translational diffusion perpendicular to the filament is also enhanced by flexibility. At times longer than rotational diffusion time ($\tau > \tau_r$) , the SWNT loses memory of its initial orientation, and its diffusion becomes isotropic. On these timescales, translational diffusion is weakly reduced by flexibility . Käs et al [45] has characterized the longitudinal diffusion constant of actin filaments in an uncrosslinked actin network. They obtained a longitudinal diffusivity ($D_\parallel \sim 1/L$) that decreased with increasing length as expected, however the absolute value was much lower than expected from the dilute solution. A large supression in the diffusivity of a stiff filament could be a result of the tortuous path the filament must follow in order to diffuse. This hypothesis can be tested by looking at the longitudinal diffusion of SWNTs with different L_p in our model system. The coordinates of the end of

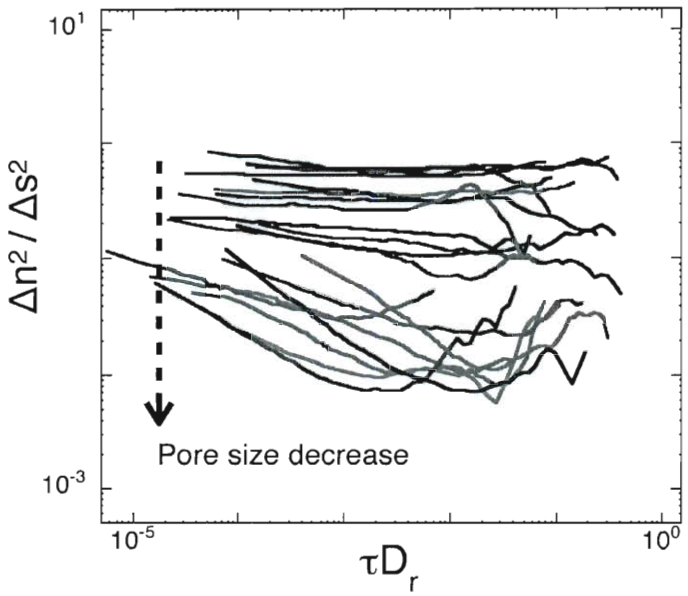

Figure 3.19 : Anisotropy between parallel and perpendicular translational diffusions increase as the pore size decrease

the skeletonized SWNT can be projected onto a one dimensional coordinate system parallel to the SWNT axis. $D_{\|}$ can be calculated from one dimensional mean square deviation $\langle x^2(\tau)\rangle \sim D_{\|}\tau$ at long timescales.

3.4 Summary

In this chapter, we established conclusively the dynamics of individual stiff filaments in crowded environments, elucidating the fundamental physics of how backbone flexibility affects mobility and diffusion. Our results clearly indicate that the SWNT shapes are altered by the presence of the pores, and that bent shapes can be very long lived. Recent advances in SWNTs surface stabilization methods could be exploited to study the issue of chemical interactions between the outer stabilization layer

on the SWNTs and the confining medium. In addition to their potential relevance for the fundamental physics of stiff polymers, the results might also be exploited in biological and technological contexts. SWNTs might be used for probing and sensing applications. By varying SWNT surface modifications, we could selectively tune the sensitivity of the carbon nanotubes to the different physical properties of the porous media for sensing applications. Rotational diffusion and coupling between translational and rotational motion of SWNTs could provide a useful counter part to translational diffusion approaches in microrheology techniques and render the ability to probe different viscoelastic modes or local heterogeneity in complex fluids and biological media.

Chapter 4

Steric stabilization of SWNTs using triblock copolymers

Single-walled carbon nanotubes (SWNTs) bundle into ropes due to strong inter-tube van der Waals attraction. Bundling damages many interesting properties of individual SWNTs and impairs utilization of SWNTs in biological and materials applications that are based on unique properties of individual SWNTs. Thus, an effective method of debundling and solubilizing nanotubes is required for SWNTs to achieve their full potential.

Polymers have proven efficient at altering the interfacial behavior of SWNTs while preserving their electronic properties. By tuning the properties of SWNT-polymer complexes, we can disperse, separate and assemble SWNTs in many different media.

Here, we introduce a simple procedure for dispersing as-produced SWNTs in aqueous solutions of triblock copolymer, poly(Styrene)-*b*-(2-Vinyl Pyridine)-*b*-(Ethyelne Oxide) (PS-*b*-P2VP-*b*-PEO). Entropic repulsion among the absorbed polymer chains generates a free energy barrier that prevents SWNTs from approaching each other too closely, i.e. within range of the attractive part of the inter-tube potential. This process yields stable aqueous dispersions of individual SWNTs without need for ultracentrifugation, thus dramatically increasing nanotube yield.

We use this SWNT/triblock copolymer system to study the effect of pH and salinity on polymer micelle conformations. We show that the SWNT suspension is stable under a wide pH range as well as high salinity environments. SWNT/triblock copoly-

mer can sequester hydrophobic and nearly hydrophobic molecules (DIB and PKH26) at very high rates. These suspensions can be used in a wide range of applications in different media where stable suspension of SWNTs is crucial.

4.1 Introduction

SWNTs are tubular structures of carbon characterized by an average diameter of about 1 nm and typical length on the order of microns and thus high aspect ratios. They have exceptional mechanical and electrical properties, ideal for many biological and materials applications. However, as-produced SWNTs usually form entangled networks of bundles or ropes, due to van der Waals attraction forces along their length [80]. When in a bundle, SWNTs are far from their optimum electronic and optical properties. Thus in order to fully exploit the properties of individual nanotube, it is crucial to develop simple debundling techniques.

Various methods have been developed for dispersing SWNTs in aqueous and organic media. These methods include covalent modifications of SWNT walls [81, 82] and non-covalent stabilization using mainly polymers [83], biopolymers [84] and surfactants [85–87]. Covalent modifications induce short ranged repulsion among the tubes but results in altered optical and electronic properties of SWNTs. Non-covalent methods, e.g., surfactant stabilization, are common for suspending SWNTs in aqueous media [87]. The stabilization mechanism relies on the interactions between surfactant molecules and SWNTs. This interaction leads to screening of the hydrophobic effects in aqueous solutions and thus dispersion of nanotubes. Although surfactant wrapped SWNTs are stable in water, slight changes in the media such as pH can destabilize SWNT-surfactant complexes leading to flocculation of SWNTs.

In aqueous dispersions, surfactant molecules bound at the SWNT surface are

in equilibrium with free surfactant molecules. Stability of surfactant suspensions is strongly dependent on surfactant concentration. SWNTs are isolated when nanotube-surfactant interactions are strong relative to surfactant-surfactant and surfactant-water interactions such that surfactant remains adsorbed and prohibits SWNTs from contacting one another and reforming van der Waals-stabilized bundles. SWNTs in stable aqueous suspensions reaggregate when the surfactant concentration is reduced substantially below the critical micelle concentration (CMC). An additional drawback recently observed in suspension of SWNTs and pluronics intended for biological application is the nonspecific exchange of the surfactant with serum proteins, which makes it undesirable for tagging purposes and other biological applications [88]. Recently a new strategy has been developed which relies on encasing the SWNTs in crosslinked polymeric micelles and produces SWNT suspensions that are stable over a wide spectrum of pH [89–91].

In all of the non-covalent methods discussed, ultracentrifugation has been carried out on the dispersions in order to remove all bundles with size above some cutoff point. This cutoff point is close to the size of an individual nanotube, resulting in dispersions rich in individual SWNTs. However, the cost of centrifugation is the loss of as much as 99% of the nanotube mass from the dispersion [4].

Here we report a cheap, simple and efficient method for dispersing SWNTs in aqueous media by encasing the nanotubes within amphiphilic triblock copolymer micelles of PS-*b*-P2VP-*b*-PEO. The advantage of this method is the production of high-quality dispersions of individual SWNTs that are stable over a wide range of pH and high salinity with no waste of nanotubes due to lack of ultracentrifugation step.

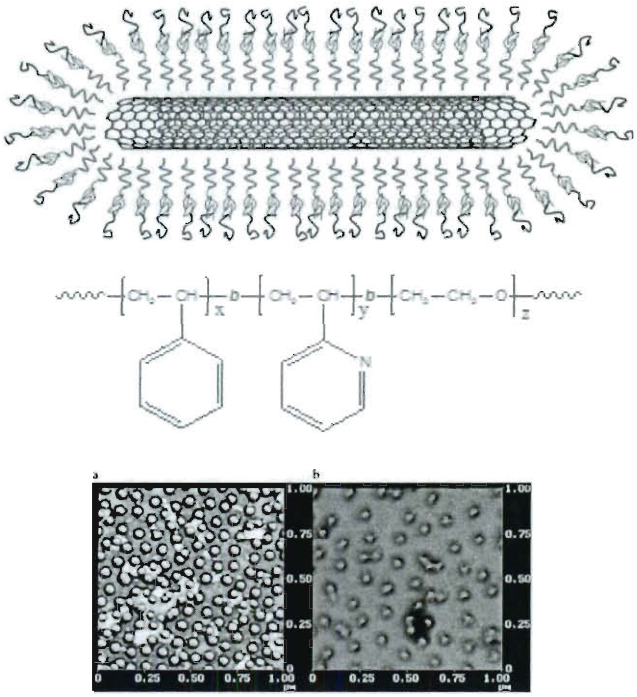

Figure 4.1 : Schematic illustration of the system. Chemical structure of the triblock copolymer. Behavior of micelles in different pH [92]

4.2 Materials and methods

4.2.1 SWNT dispersion

Amphiphilic PS-*b*-P2VP-*b*-PEO (4.1) was obtained from Polymer Source Inc., Dorval, Canada. (Mn = 3.2-b-1.3-b-3.0 $\times 10^3$). In a typical experiment triblock copolymer was first dissolved in dimethylformamide (DMF), a solvent in which all blocks are soluble and no micelle formation is induced (1 wt/wt % solution of triblock copolymer in DMF). A few mg of raw SWNTs (HiPco, batch number 162.5) were added to 1 mL of polymer solution and exfoliated via ultra tip sonication (or bath sonication (5-10 Watts)) for 20 minutes. 10 mL of deionized water was added slowly at a rate of 0.1

mL/min (via a syringe pump) to the SWNTs-polymer-DMF solution. The sample was kept an ice bath to prevent heating. After the sonication no chunks of SWNTs were visible with optical microscopy. Thus, no centrifugation step was performed.

4.2.2 Characterization

Atomic force microscopy (AFM) images were obtained using a Nanoscope IIIa (Digital Instruments/Veeco Metrology, Inc., Santa Barbara, CA) instrument, operating in tapping mode at a scan rate of 2 Hz. Samples for AFM analysis were prepared by spin-coating 20 μL of SWNT suspensions onto freshly cleaved mica surfaces (Ted Pella, Inc., Redding, CA) and rinsing with DMF and 2-isopropanol to remove the excess of polymer. Samples were dried thoroughly before scanning.

Liquid phase Raman spectroscopy was performed using a 785 nm laser excitation in a Renishaw system fitted with a microscope. Spectra were collected between 100 and 3200 cm^{-1} (with 10 s exposure time and 1 accumulation).

Bulk fluorescence and absorbance measurements were measured with a Nanospectralyzer Model NS1, Version 1.97 (Applied Nanofluorescence, Houston, Texas, USA). The SWNT fluorescence was excited at 660 nm and 785 nm and emission was detected between 900 and 1400 nm. Absorbance was measured in the visible and near infrared (400 to 1400 nm) (with integration time 500 ms and 10 accumulations).

4.3 Results

4.3.1 SWNT/triblock copolymer complex

Block copolymers consist of distinct segments with dual action: while one of the blocks anchors the chain to the surface, the other block protrudes into the solvent

where it is thermally mobile. When another surface comes close, the reduction in the entropy of these mobile blocks due to confinement results in a repulsive force known as steric repulsion and thus prevents flocculation.

The method for dispersing SWNTs in amphiphilic block copolymer follows the methodology demonstrated for forming multilayered assemblies known as core-shell-corona (CSC) micelles in water [92, 93]. These micelles consists of a PS core, a pH-responsive P2VP shell, and a PEO corona. The pyridine units in the P2VP block are Brϕnsted bases. Acids can react with pyridines by protonating the pyridine units. At pH values below 5, they are protonated and adopt a stretched conformation because of the mutual electrostatic repulsions while at pH values above 5, the P2VP blocks are hydrophobic and collapse on the PS core. Micelle formation is triggered by addition of a small amount of water into a dilute solution of the copolymer in a non-selective organic solvent.

Amphiphilic PS-*b*-P2VP-*b*-PEO (4.1) was first dissolved in dimethylformamide (DMF), a solvent in which all blocks are soluble and no micelle formation is induced. SWNTs were added to the polymer solution and exfoliated via ultrasonication (or bath sonication). Water, which is miscible with DMF in all proportions, was then slowly added to the SWNTs-polymer-DMF solution in order to decrease the solvent power toward PS and P2VP. Thus, as soon as the DMF-H_2O composition was such that the solvent mixture was a θ solvent for the hydrophobic blocks, phase separation occurred. The slow addition of the first mL of water was critical, because at the beginning these micelles were highly unstable and ill shaped. The immediate addition of water possibly causes formation of empty (no SWNTs inside) and frozen micelles due to the formation of glassy cores at a specific nonselective solvent / selective solvent composition. When enough water has been added that the glass-transition

temperature of the DMF swollen core (PS) exceeds the ambient temperature and that the shape, size, and aggregation number of the micelles are defined. The glassy core of PS encased the hydrophobic SWNT. The further expulsion of DMF from the micellar PS core and the collapsed P2VP shell forces the hydrophilic PEO chains to stretch, extending into water to impart solubility and to prevent re-aggregation of SWNTs.

The nanostructure of SWNTs encased within PS-*b*-P2VP-*b*-PEO micelles was characterized by atomic force microscopy (AFM), UV-Vis, fluorescence and liquid-phase Raman spectroscopy.

In order to characterize the state of the nanotubes at the nanoscale we examine deposited samples with tapping-mode AFM (figure 4.2).

The images reveal that the majority of SWNTs are individuals or small bundles (figure 4.3).

When the absorbing species are SWNTs, UV-vis gives information on the sample composition of both metallic and semiconductors. The concentration (in mg/L) of SWNTs suspensions was determinate by dividing the optical absorbance value at 763 nm by 0.043 (typical concentration values of 20-40 mg/L).

Photoluminescence (PL) spectroscopy

One of the important properties of SWNTs is the NIR fluorescence of the individual semiconducting nanotubes [4,5]. The intensity and the wavelength of the fluorescence are highly sensitive to the surrounding environment which can be utilized for sensing/ characterizing purposes.

Here, photoluminescence (PL) spectroscopy was used to infer the effectiveness of the triblock copolymer at breaking up the bundles of nanotubes and dispersing them

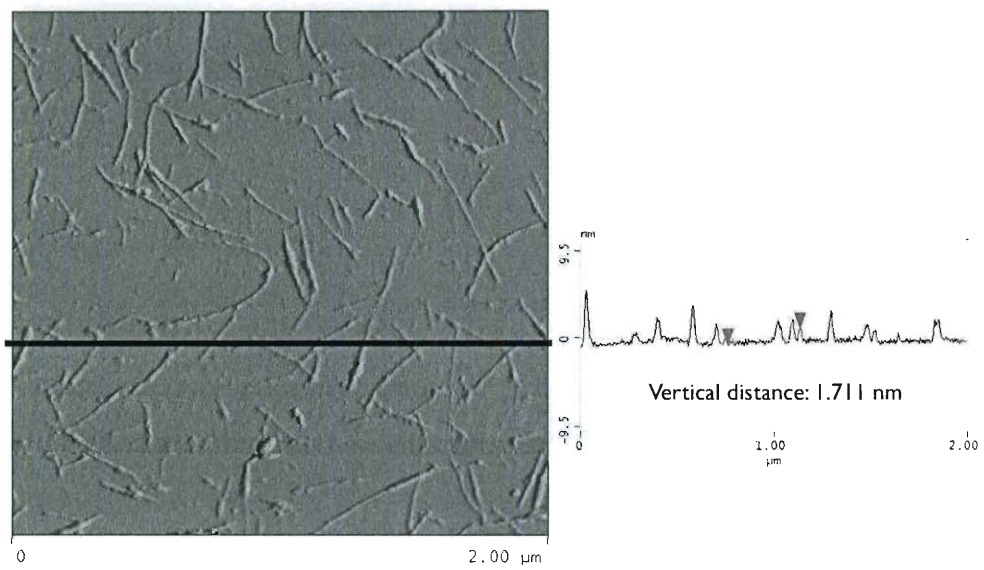

Figure 4.2 : AFM images of SWNT/triblock copolymer, apparent height 1.8 nm

as individuals. Metallic SWNTs (about a third of all SWNTs in any bulk sample) act as non-radiative decay pathways for any photo excited carriers in a SWNT bundle, therefore the PL intensity is proportional to the number of individual SWNTs in the dispersion. [94]

Figure 4.4) shows the photoluminescence (660 nm and 785 nm excitation wavelength) of the bulk SWNT suspensions (the sample consisted of SWNTs, triblock copolymer, water and DMF) right after sonication but with no centrifugation step in comparison with SWNT/SDBS and SWNT/pluronics (F88) of similar concentration undergoing 4 hours of ultracentrifugation.

The low PL quantum yields in comparison with SWNT-SDBS dispersion is most

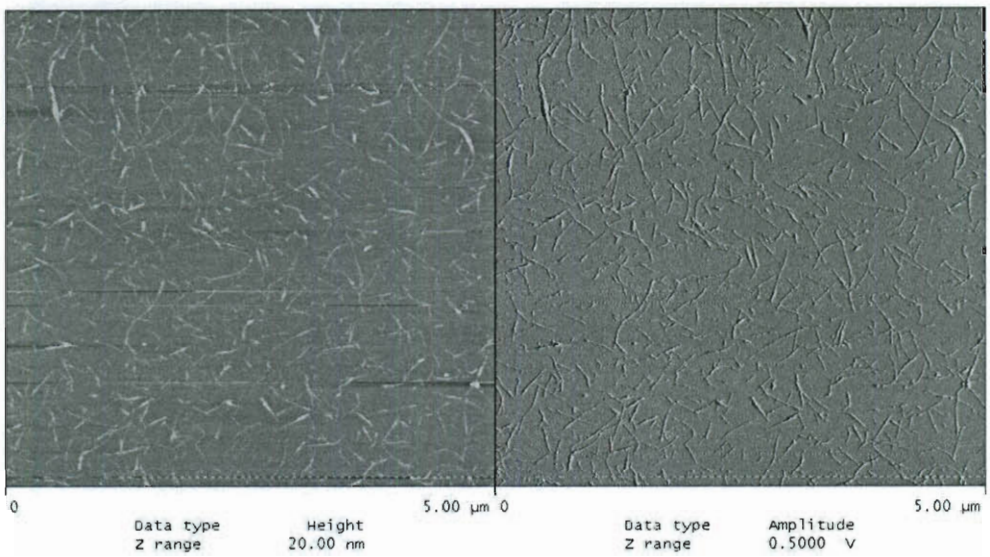

Figure 4.3 : AFM images of SWNT/triblock copolymer reveal the majority of SWNTs are individuals or small bundles

likely associated with the presence of small nanotube bundles (also evident from AFM images). In addition, the broadening of spectral features and a 30 nm red shift of emission lines (figure 4.5) indicate a change in the dielectric environment. Bundling of SWNTs yield in a small increase of the dielectric function which account for the observed red shifts. However, it is noteworthy that no centrifugation step has been carried out to remove the bundles.

In order to further study the degree of bundling, Raman spectroscopy was performed. The liquid-phase Raman spectra of the suspension using 785 nm excitation laser which selectively excites semiconducting nanotubes with diameters near 1 nm is shown in figure 4.6. The degree of bundling can be identified by comparing the

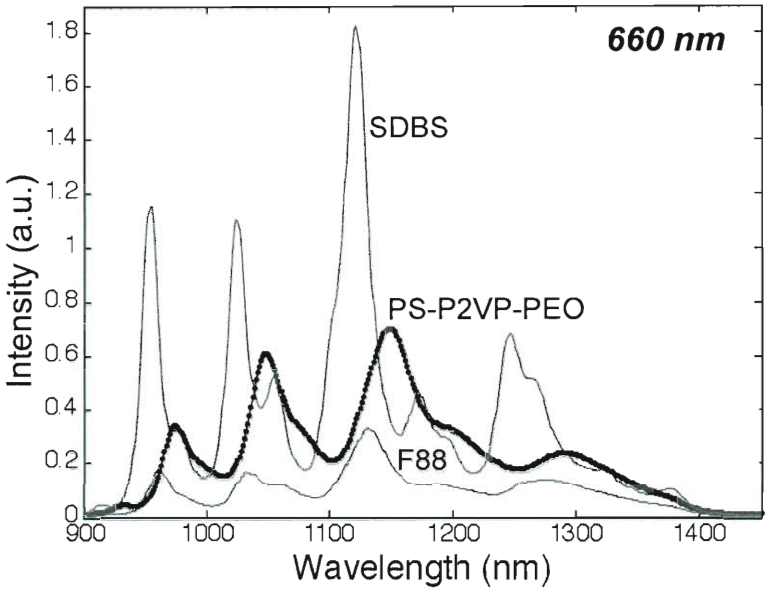

(a) 660nm

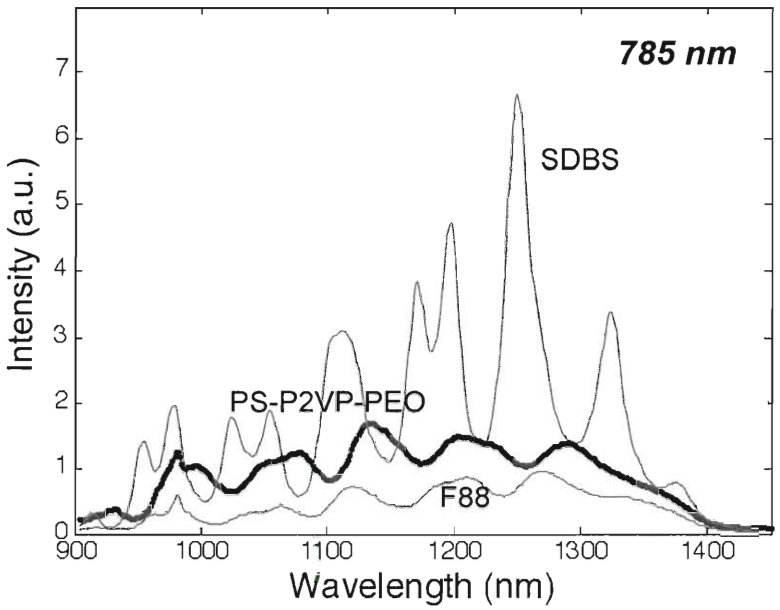

(b) 785nm

Figure 4.4 : The fluorescence of SWNT/polymer in comparison with SDBS and F88

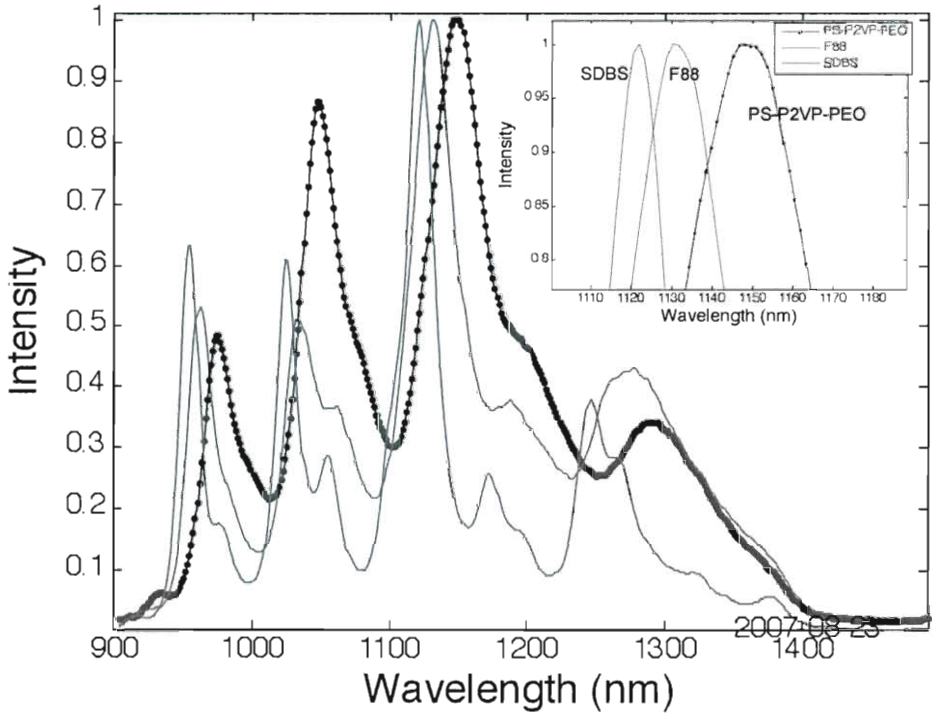

Figure 4.5 : Fluorescence spectra line shift

area under the RBM of individual semiconducting SWNTs (150 to 250 cm^{-1}) with that of SWNT that are brought into resonance with the laser due to the presence of SWNT bundles (250-300 cm^{-1}) [95]. The bundling peak (250-300 cm^{-1}), is fairly small considering no centrifugation step has been carried out (figure 4.7).

4.3.2 Stability of SWNT-polymer complex

Dialysis

Dialysis against water for 24 hours using a 50K dialysis bag ensured the removal of DMF and a completely aqueous solution. The samples were stable despite vigorous dialysis against water evident from no change (decrease or shift) in fluorescence

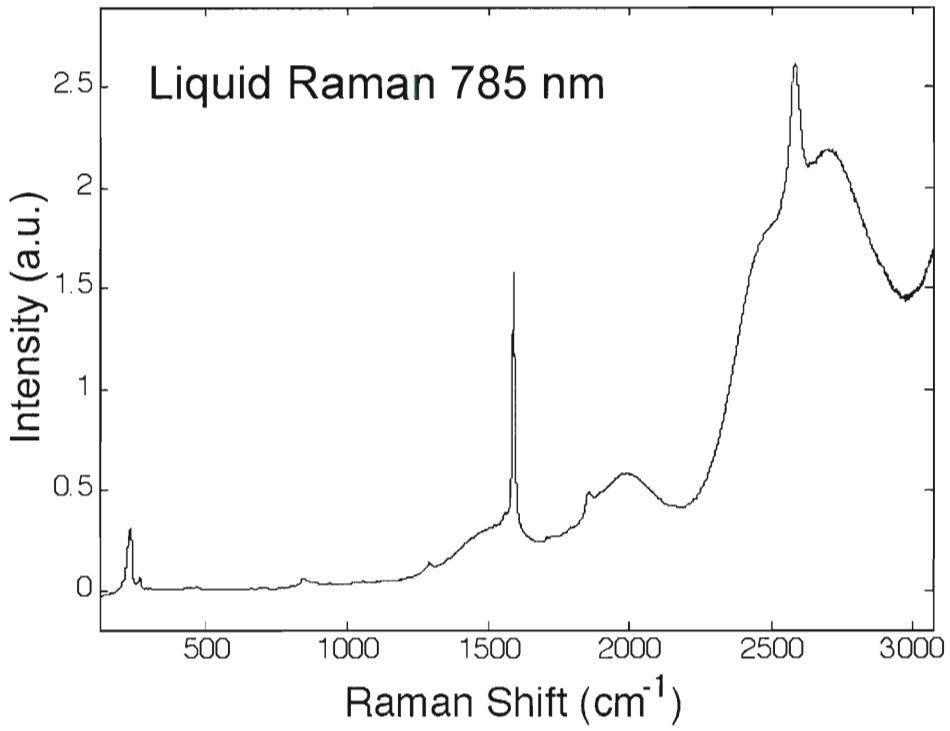

Figure 4.6 : Liquid-phase Raman with 785 nm excitation wavelength

emission line (figure 4.8) as well as constant bundling peak in the Raman spectrum. This shows that micelles encasing SWNTs are kinetically frozen out of equilibrium, particularly due to the fact that the poly(styrene) core is glassy (glass transition temperature, $T_g \sim 100°C$ for bulk polystyrene) and that there are strong interactions between PS block and SWNT surface. This triblock copolymer acts very differently from soft (low T_g) triblock polymers such as pluronics; The pluronics are prone to re-organization when exposed to external stimuli, given their low T_g.

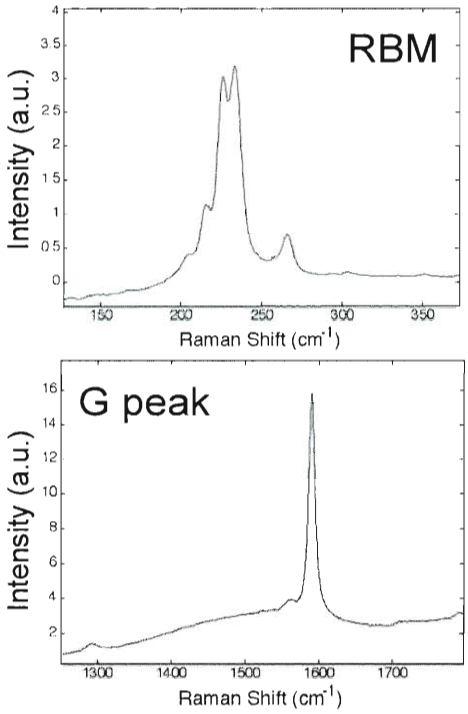

Figure 4.7 : RBM and G peaks in Raman spectrum

Effect of pH and salinity

Furthermore, in order to test the stability of the sample, the fluorescence spectra of the sample were monitored while inducing pH changes in the suspensions. Figure 4.10 shows the PL intensity of the triblock/SWNTs suspensions is fairly stable along the pH range. However, we do note the slight decreases from alkaline (pH 11) to acidic (pH 1) conditions and the slight redshift of the spectrum. But this is somewhat counter-intuitive because acids can react with pyridines by protonating the pyridine units. At pH values below 5, they are protonated and adopt a stretched conformation because of the mutual electrostatic repulsions while at pH values above 5, the P2VP blocks are hydrophobic and collapse on the PS core [93]. So one would expect to see

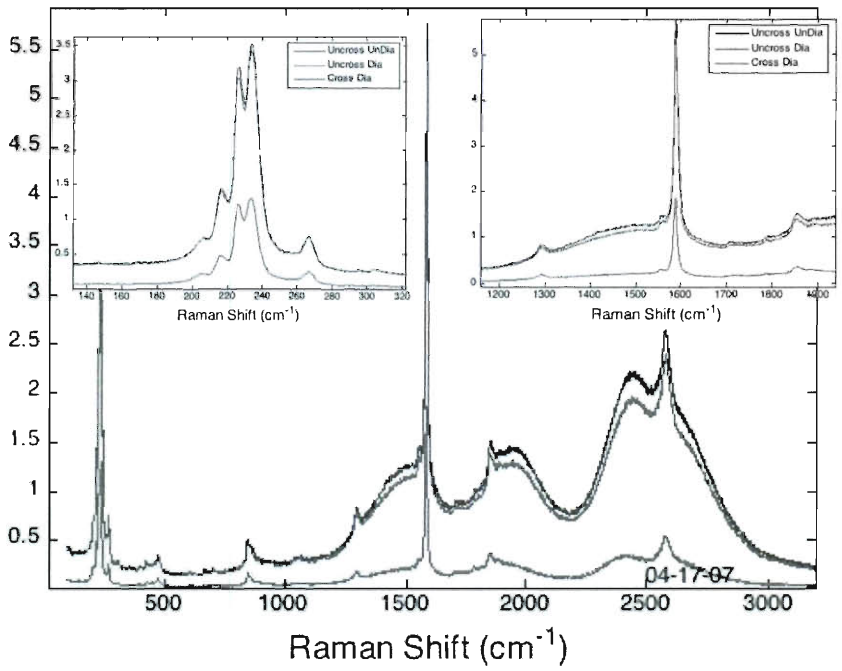

Figure 4.8 : Liquid-phase Raman of sample after dialysis and after crosslinking

higher PL intensities in higher pH because we have both a glassy core of PS as well as a collapsed P2VP shell, so the SWNTs should be very well shielded.

We also tested the stability of the suspensions in high salinity solutions: SWNT/polymer suspensions were diluted in 10x phosphate buffered saline (PBS). The suspension stability and the luminescence were not affected in such high salinity medium evident by the steady fluorescence intensity levels of the (7,6) peak as a function of time (normalized to the initial condition at pH 7). Thus these suspensions would be highly desirable for application in biological environments as well as environments with high salinity conditions.

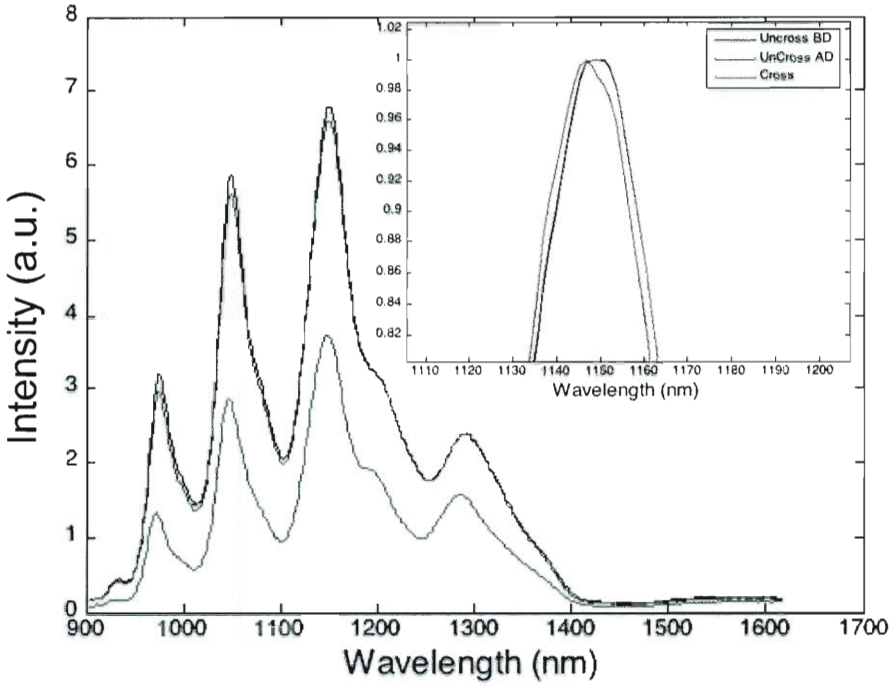

Figure 4.9 : Photoluminescence quenching after addition of crosslinker

4.3.3 Shell crosslinking

The triblock copolymer was crosslinked around the SWNT by reacting the P2VP shell with a crosslinker. This modification suppresses the unimer-micelle equilibrium and creates shells that virtually consist of one molecule after cross-linking.

The P2VP block of the polymer was crosslinked by quaternization with 1,4-Diiodobutane (DIB), which is a hydrophobic molecule [96]. 1 mole crosslinker per 2 moles of VP was added to the dialyzed SWNT/triblock polymer aqueous solution and then the sample was bath sonicated for 30 sec. Quaternization of P2VP has a very slow reaction rate under ambient condition ($\sim$ several hours to days) and is characterized by a change in solution color from clear to opaque light-yellow [97]. In our

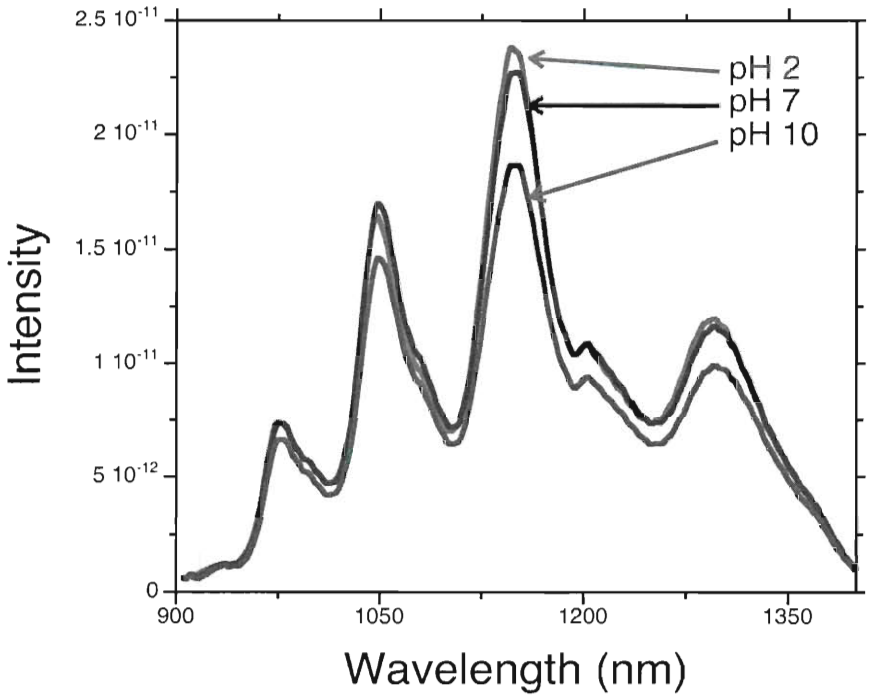

Figure 4.10 : Effect of pH on Photoluminescence of SWNT/triblock solution

experiment, only after 30 seconds of bath sonication the color of the solution changed from clear to pale yellow. Quaternization was further confirmed by the disappearance of the 1369 and 1303 cm^{-1} aromatic C-N stretching vibrations in the Fourier transform infrared (FTIR) spectrum (Nicolet FTIR Infrared Microscope) [97].

To explain such extraordinary acceleration in the crosslinking reaction rate we propose the possibility of DIB sequestration by the assembled PEO-*b*-P2VP-*b*-PS around SWNTs: the SWNT/triblock copolymer uptake and sequester the DIB molecules in their hydrophobic interior. This hypothesis was further tested by dissolving pyridine in water at a similar concentration to PEO-*b*-P2VP-*b*-PS followed by adding the same amount of DIB and sonicating it for 30 sec. There was no visible sign of reaction, even

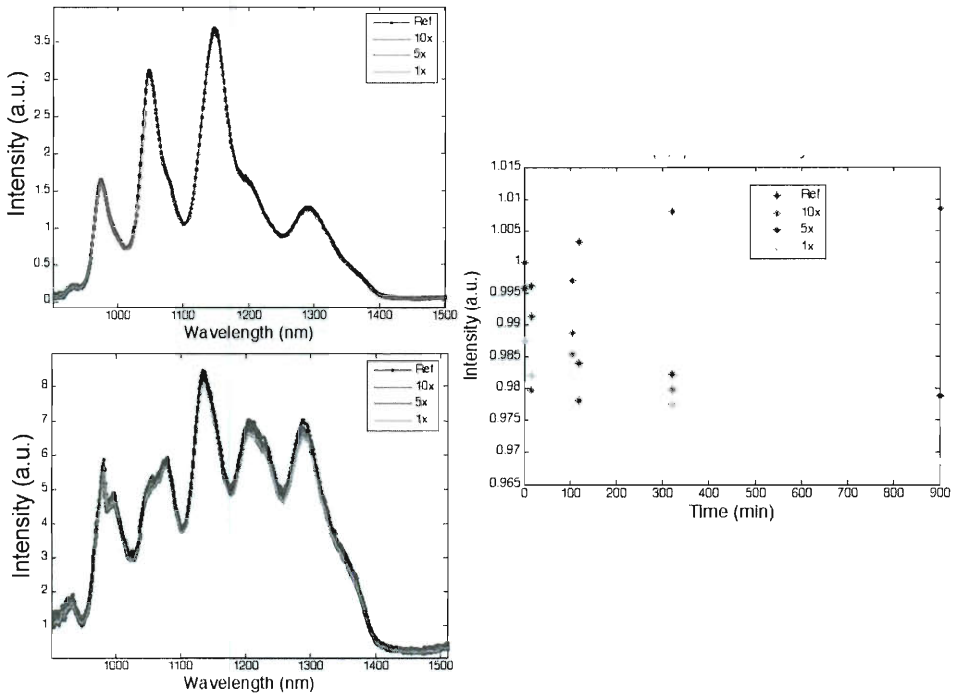

Figure 4.11 : Stability in high salinity

after days. Interestingly, such fast reaction rate has not been observed in assembled films or micelles of this triblock copolymer [97].

Figure 4.10 displays the fluorescence spectra of crosslinked SWNT-triblock copolymer in comparison to that of uncrosslinked and dialyzed SWNT/triblock copolymer suspensions. A decrease in fluorescence intensity is noticed. Interestingly, a slight blueshift (a few nm) was observed in the sample of crosslinked sample, which could be due to a change in dielectric constant of the SWNTs surrounding ($\Delta E \propto \epsilon^{-1}$ where ϵ is the dielecric constant). To complement these observations, the liquid-phase Raman spectra of the suspensions were also measured (4.11). A decrease in Raman intensity is due to scattering from the crosslinked sample. The degree of bundling,

was unchanged because the bundling peak remained constant.

4.3.4 Incorporation of dye molecules in the micelle structure

Visualization of SWNTs in water by fluorescence microscopy can be accomplished by adding a small amount of hydrophobic dye (PKH26, Sigma, excitation 551 nm and emission 567 nm) to a solution of the dispersed SWNTs/surfactants [16]. Such a dye molecule partitions into the hydrophobic core of the surfactant assemblies around SWNTs and therefore SWNTs can be directly observed under the microscope.

Using this approach, we labeled the un-crosslinked SWNT-triblock copolymer complexes with PKH26 by mixing 10 μL of the aqueous SWNT suspension with 1 μL of the dye and vortex mixing for 1 min. The SWNT-copolymer structure can uptake and sequester the dye molecules in their hydrophobic interior. For visualization 2 μL suspension of labelled SWNTs was placed on hydrophilic glass (soaked for 30 minutes in a mixture of 70 % sulfuric acid and 30 % hydrogen peroxide, rinsed with water and wiped clean with methanol) and then covered with a hydrophilic coverslip.

Images were acquired on a Nikon E600 epi-fluorescence microscope with a XF37 filter cube (Omega Optical, Inc., USA ; excitation 540-550 / 555 dichroic / emission 570-600 nm), a 100X oil immersion objective (N.A.=1.4, depth of focus 0.5 μm), and an electron-bombarded CCD video camera (Hamamatsu, Japan), controlled by MetaMorph software (Universal Imaging Co., USA).

Figure 4.12 shows an image of fluorescently labeled SWNTs/triblock copolymer.

4.4 Conclusion

In conclusion, we have produced stable dispersions of SWNT suspended using PS-*b*-P2VP-*b*-PEO triblock copolymer in water. The SWNTs are in the form of individuals

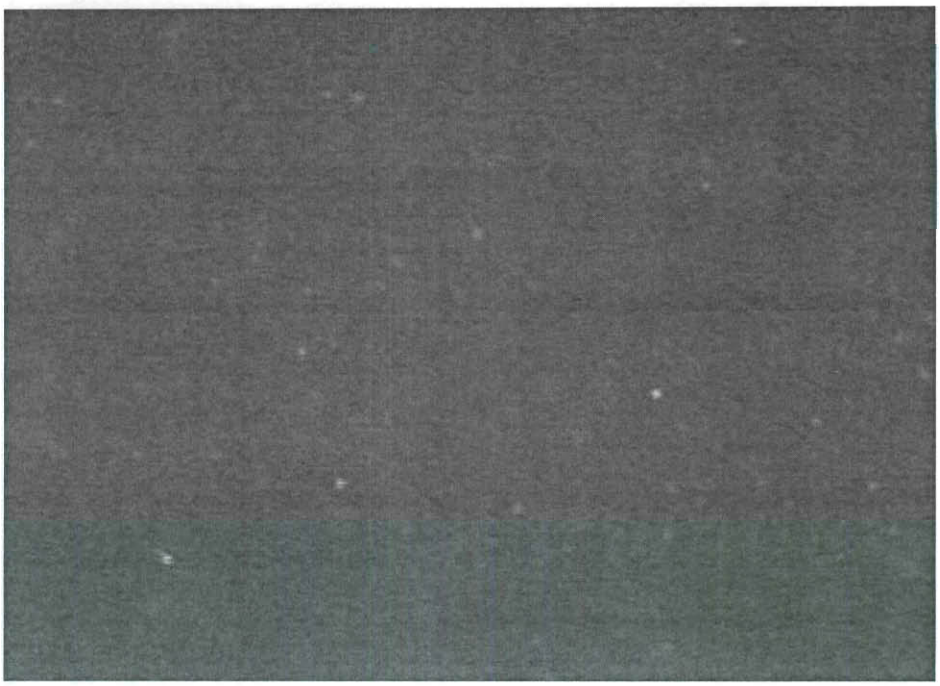

Figure 4.12 : Fluorescent image of SWNTs/polymer/dye complex

and small bundles with no aggregates. This has been achieved without the need for ultracentrifugation. The suspension is stable under a wide pH range as well as high salinity environments. We have shown that SWNT-triblock copolymer is capable of sequestering hydrophobic molecules (DIB and PKH26) at very high rates. These suspensions can be used in a wide range of applications in different media where stable suspension of SWNTs is crucial.

Triblock copolymers encasing the SWNT introduce a steric barrier that can be tuned by altering polymer chain length and surface density. This system or any SWNT-polymer complex can be excellent model systems to study interfacial behavior such as the strength and range of polymer induced steric repulsion by probing the

unique PL properties of SWNTs.

Bibliography

[1] M Doi and S.F. Edwards. *The Theory of Polymer Dynamics.* International Series of Monographs on Physics. Oxford University Press, Oxford, 1986.

[2] T T Perkins, D E Smith, and S Chu. Direct observation of tube-like motion of a single polymer chain. *Science*, 264(5160):819–22, 1994.

[3] J Käs, H Strey, and E Sackmann. Direct imaging of reptation for semiflexible actin filaments. *Nature*, 368(6468):226–9, 1994.

[4] M. J. O'Connell, S. M. Bachilo, C. B. Huffman, V. C. Moore, M. S. Strano, E. H. Haroz, K. L. Rialon, P. J. Boul, W. H. Noon, C. Kittrell, J. P. Ma, R. H. Hauge, R. B. Weisman, and R. E. Smalley. Band gap fluorescence from individual single-walled carbon nanotubes. *Science*, 297(5581):593–596, 2002.

[5] S. M. Bachilo, M. S. Strano, C. Kittrell, R. H. Hauge, R. E. Smalley, and R. B. Weisman. Structure-assigned optical spectra of single-walled carbon nanotubes. *Science*, 298:2361–2366, 2002.

[6] D. A. Tsyboulski, S. M. Bachilo, and R. B. Weisman. Versatile visualization of individual single-walled carbon nanotubes with near-infrared fluorescence microscopy. *Nano Letters*, 5:975–979, 2005.

[7] R Baughman, A Zakhidov, and W de Heer. Carbon nanotubes-the route toward applications. *Science*, 297(5582):787–792, 2002.

[8] S. Polizu, O. Savadogo, P. Poulin, and L. Yahia. Applications of carbon nanotubes-based biomaterials in biomedical nanotechnology. *Journal of Nanoscience and Nanotechnology*, 6:1883–1904, 2006.

[9] N. Geblinger, A. Ismach, and E. Joselevich. Self-organized nanotube serpentines. *Nature Nanotechnology*, 3:195–200, 2008.

[10] V. A. Davis, L. M. Ericson, A. N. G. Parra-Vasquez, H. Fan, Y. H. Wang, V. Prieto, J. A. Longoria, S. Ramesh, R. K. Saini, C. Kittrell, W. E. Billups, W. W. Adams, R. H. Hauge, R. E. Smalley, and M. Pasquali. Phase behavior and rheology of swnts in superacids. *Macromolecules*, 37:154–160, 2004.

[11] P. M. Ajayan and J. M. Tour. Materials science - nanotube composites. *Nature*, 447:1066–1068, 2007.

[12] S. Kumar, T. D. Dang, F. E. Arnold, A. R. Bhattacharyya, B. G. Min, X. F. Zhang, R. A. Vaia, C. Park, W. W. Adams, R. H. Hauge, R. E. Smalley, S. Ramesh, and P. A. Willis. Synthesis, structure, and properties of pbo/swnt composites. *Macromolecules*, 35:9039–9043, 2002.

[13] M. Sano, A. Kamino, J. Okamura, and S. Shinkai. Ring closure of carbon nanotubes. *Science*, 293:1299–1301, 2001.

[14] W. Zhou, M. F. Islam, H. Wang, D. L. Ho, A. G. Yodh, K. I. Winey, and J. E. Fischer. Small angle neutron scattering from single-wall carbon nanotube suspensions: Evidence for isolated rigid rods and rod networks. *Chemical Physics Letters*, 384:185–189, 2004.

[15] D. W. Schaefer, J. Zhao, J. M. Brown, D. P. Anderson, and D. W. Tomlin. Morphology of dispersed carbon single-walled nanotubes. *Chemical Physics Letters*,

375:369–375, 2003.

[16] R. Duggal and M. Pasquali. Dynamics of individual single-walled carbon nanotubes in water by real-time visualization. *Physical Review Letters*, 96(24):246104, 2006.

[17] K. N. Kudin, G. E. Scuseria, and B. I. Yakobson. C2f, bn, and c nanoshell elasticity from ab initio computations. *Physical Review B*, 64:235406, 2001.

[18] B. I. Yakobson and L. S. Couchman. Persistence length and nanomechanics of random bundles of nanotubes. *Journal of Nanoparticle Research*, 8:105–110, 2006.

[19] C. P. Brangwynne, G. H. Koenderink, E. Barry, Z. Dogic, F. C. MacKintosh, and D. A. Weitz. Bending dynamics of fluctuating biopolymers probed by automated high-resolution filament tracking. *Biophysical Journal*, 93:346–359, 2007.

[20] F. Gittes, B. Mickey, J. Nettleton, and J. Howard. Flexural rigidity of microtubules and actin-filaments measured from thermal fluctuations in shape. *Journal of Cell Biology*, 120:923–934, 1993.

[21] M. E. Janson and M. Dogterom. A bending mode analysis for growing microtubules: Evidence for a velocity-dependent rigidity. *Biophysical Journal*, 87:2723–2736, 2004.

[22] A. Ott, M. Magnasco, A. Simon, and A. Libchaber. Measurement of the persistence length of polymerized actin using fluorescence microscopy. *Physical Review E*, 48:R1642–R1645, 1993.

[23] D. A. Tsyboulski, J. D. R. Rocha, S. M. Bachilo, L. Cognet, and R. B. Weisman. Structure-dependent fluorescence efficiencies of individual single-walled cardon nanotubes. *Nano Letters*, 7:3080–3085, 2007.

[24] S. R. Aragon and R. Pecora. Dynamics of wormlike chains. *Macromolecules*, 18:1868–1875, 1985.

[25] V. Shankar, M. Pasquali, and D. C. Morse. Theory of linear viscoelasticity of semiflexible rods in dilute solution. *Journal of Rheology*, 46:1111–1154, 2002.

[26] F. Gittes and F. C. MacKintosh. Dynamic shear modulus of a semiflexible polymer network. *Physical Review E*, 58(2):R1241–R1244, 1998.

[27] G. L. Li and J. X. Tang. Diffusion of actin filaments within a thin layer between two walls. *Physical Review E*, 69:061921, 2004.

[28] T. Odijk. Polyelectrolytes near the rod limit. *Journal of Polymer Science: Polymer Physics Edition*, 15:477–483, 1977.

[29] J. Skolnick and M. Fixman. Electrostatic persistence length of a wormlike polyelectrolyte. *Macromolecules*, 10:944–948, 1977.

[30] M. Pasquali, V. Shankar, and D. C. Morse. Viscoelasticity of dilute solutions of semiflexible polymers. *Physical Review E*, 64(2):020802, 2001.

[31] M. M. A. E. Claessens, M. Bathe, E. Frey, and A. R. Bausch. Actin-binding proteins sensitively mediate f-actin bundle stiffness. *Nature Materials*, 5:748–753, 2006.

[32] N. Behabtu, M. J. Green, and M. Pasquali. Carbon nanotube-based neat fibers. *Nano Today*, 3:24–34, 2008.

[33] M. Motta, A. Moisala, I. A. Kinloch, and A. H. Windle. High performance fibres from 'dog bone' carbon nanotubes. *Advanced Materials*, 19:3721–3726, 2007.

[34] J. A. Elliott, J. K. W. Sandler, A. H. Windle, R. J. Young, and M. S. P. Shaffer. Collapse of single-wall carbon nanotubes is diameter dependent. *Physical Review Letters*, 92:095501, 2004.

[35] U. J. Kim, H. R. Gutierrez, J. P. Kim, and P. C. Eklund. Effect of the tube diameter distribution on the high-temperature structural modification of bundled single-walled carbon nanotubes. *Journal of Physical Chemistry B*, 109:23358–23365, 2005.

[36] D. A. Tsyboulski, S. M. Bachilo, A. B. Kolomeisky, and R. B. Weisman. Translational and rotational dynamics of individual single-walled carbon nanotubes in aqueous suspension. *ACS Nano*, 2(9):1770–6, 2008.

[37] P. K. Rai, A. N. G. Parra-Vasquez, J. Chattopadhyay, R. A. Pinnick, F. Liang, A. K. Sadana, R. H. Hauge, W. E. Billups, and M. Pasquali. Dispersions of functionalized single-walled carbon nanotubes in strong acids: Solubility and rheology. *Journal of Nanoscience and Nanotechnology*, 7:3378–3385, 2007.

[38] M. S. Arnold, S. I. Stupp, and M. C. Hersam. Enrichment of single-walled carbon nanotubes by diameter in density gradients. *Nano Letters*, 5:713–718, 2005.

[39] T Odijk. On the statistics and dynamics of confined or entangled stiff polymers. *Macromolecules*, 16(8):1340–1344, 1983.

[40] M. Doi and S. F. Edwards. Dynamics of concentrated polymer systems .1. brownian-motion in equilibrium state. *Journal of the Chemical Society-Faraday Transactions II*, 74:1789–1801, 1978.

[41] S. F. Edwards. Statistical mechanics of polymerized material. *Proceedings of the Physical Society of London*, 92(575P):9, 1967.

[42] P. G. de Gennes. Reptation of a polymer chain in presence of fixed obstacles. *Journal of Chemical Physics*, 55(2):572–579, 1971.

[43] T P Lodge, N A Rotstein, and S Prager. *Dynamics of Entangled Polymer Liquids: Do Linear Chains Reptate?*, volume 79 of *Advances in Chemical Physics*. John Wiley and Sons, 1990.

[44] J. Higgins and T. McLeish. Travelling by tube. *Nature*, 365(6443):205–206, 1993.

[45] J Käs, H Strey, J X Tang, D Finger, R Ezzell, E Sackmann, and P A Janmey. F-actin, a model polymer for semiflexible chains in dilute, semidilute, and liquid crystalline solutions. *Biophysical Journal*, 70(2):609–25, 1996.

[46] M. Doi. Rotational relaxation-time of rigid rod-like macromolecule in concentrated solution. *Journal de Physique*, 36(7-8):607–611, 1975.

[47] M.A. Tracy and R. Pecora. Dynamics of rigid and semirigid rodlike polymers. *Annual Review of Physical Chemistry*, 43:525–557, 1992.

[48] K. M. Zero and R. Pecora. Rotational and translational diffusion in semidilute solutions of rigid-rod macromolecules. *Macromolecules*, 15(1):87–93, 1982.

[49] F. Hofling, T. Munk, E. Frey, and T. Franosch. Entangled dynamics of a stiff polymer. *Physical Review E*, 77(6):060904(R), 2008.

[50] GT Keep and R Pecora. Reevaluayion of the dynamic-model for rotational diffusion of thin, rigid rods in semidilute solution. *Macromolecules*, 18(6):1167–1173,

1985.

[51] N. Ookubo and R. Hayakawa. Molecular theory on the entanglement effect of rodlike polymers. *Physical Review Letters*, 55(24):2712–2715, 1985.

[52] G. T. Keep and R. Pecora. Dynamics of rodlike macromolecules in nondilute solutions - poly(normal-alkyl isocyanates). *Macromolecules*, 21(3):817–829, 1988.

[53] S. F. Edwards and K. E. Evans. Dynamics of highly entangled rod-like molecules. *Journal of the Chemical Society-Faraday Transactions II*, 78:113–121, 1982.

[54] T. Sato, Y. Takada, and A. Teramoto. Dynamics of stiff-chain polymers in isotropic solution .3. flexibility effect. *Macromolecules*, 24(23):6220–6226, 1991.

[55] S. S. Wijmenga and A. Maxwell. Rotational diffusion of short dna fragments in polyacrylamide gels: An electric birefringence study. *Biopolymers*, 25(11):2173–2186, 1986.

[56] M. J. Green, N. Behabtu, and M. Pasquali. Nanotubes as polymers. *Polymer*, 50(21):4979–4997, 2009.

[57] N. Fakhri, D. A. Tsyboulski, L. Cognet, R. B. Weisman, and M. Pasquali. Diameter-dependent bending dynamics of single-walled carbon nanotubes in liquids. *Proceedings of the National Academy of Sciences of the United States of America*, 106(34):14219–23, 2009.

[58] A. H. Clark, R. K. Richardson, S. B. Rossmurphy, and J. M. Stubbs. Structural and mechanical-properties of agar gelatin co-gels - small-deformation studies. *Macromolecules*, 16(8):1367–1374, 1983.

[59] J. D. Ferry. *Viscoelastic Properties of Polymers.* John Wiley and Sons, third edition, 1980.

[60] Thor L. Smith. *Molecular Aspects of Rubber Elasticity*, volume 10 of *Treatise on Materials Science and Technology.* Academic Press, 1977.

[61] P. J. Flory. Molecular size distribution in three dimensional polymers. ii. trifunctional branching units. *Journal of the American Chemical Society*, 63:3091–3096, 1941.

[62] P. J. Flory. Molecular size distribution in three dimensional polymers. i. gelation. *Journal of the American Chemical Society*, 63:3083–3090, 1941.

[63] M. T. Valentine, P. D. Kaplan, D. Thota, Crocker J. C., T. Gisler, R. K. Prud'homme, M. Beck, and D. A. Weitz. Investigating the microenvironments of inhomogeneous soft materials with multiple particle tracking. *Physical Review E*, 64:061506, 2001.

[64] P. G. de Gennes. Dynamics of entangled polymer-solutions .1. rouse model. *Macromolecules*, 9(4):587–593, 1976.

[65] P. G. de Gennes. Dynamics of entangled polymer-solutions .2. inclusion of hydrodynamic interactions. *Macromolecules*, 9(4):594–598, 1976.

[66] P. G. de Gennes. *Scaling Concepts in Polymer Physics.* Cornell University Press, 1979.

[67] T. Tanaka, Y. Urabe, D. Nishide, and H. Kataura. Continuous separation of metallic and semiconducting carbon nanotubes using agarose gel. *Applied Physics Express*, 2(12):125002, 2009.

[68] S. Badaire, P. Poulin, M. Maugey, and C. Zakri. In situ measurements of nanotube dimensions in suspensions by depolarized dynamic light scattering. *Langmuir*, 20(24):10367–10370, 2004.

[69] S. S. Work and D. M. Warshaw. Computer-assisted tracking of actin filament motility. *Analytical Biochemistry*, 202(2):275–285, 1992.

[70] S. Badaire, P. Poulin, M. Maugey, and C. Zakri. In situ measurements of nanotube dimensions in suspensions by depolarized dynamic light scattering. *Langmuir*, 20(24):10367–10370, 2004.

[71] Y Han, A. M Alsayed, M Nobili, J Zhang, T. C Lubensky, and A. G Yodh. Brownian motion of an ellipsoid. *Science*, 314(5799):626–630, 2006.

[72] L. Cognet, D. A. Tsyboulski, J. D. R. Rocha, C. D. Doyle, J. M. Tour, and R. B. Weisman. Stepwise quenching of exciton fluorescence in carbon nanotubes by single-molecule reactions. *Science*, 316(5830):1465–1468, 2007.

[73] N. Pernodet, M. Maaloum, and B. Tinland. Pore size of agarose gels by atomic force microscopy. *Electrophoresis*, 18(1):55–58, 1997.

[74] D. C. Morse. Viscoelasticity of concentrated isotropic solutions of semiflexible polymers. 2. linear response. *Macromolecules*, 31(20):7044–7067, 1998.

[75] A Semenov. Dynamics of concentrated solutions of rigid-chain polymers. part 1. brownian motion of persistent macromolecules in isotropic solution. *Journal of the Chemical Society-Faraday Transactions II*, 82:317–329, 1986.

[76] E. Farge and A. C. Maggs. Dynamic scattering from semiflexible polymers. *Macromolecules*, 26(19):5041–5044, 1993.

[77] R Granek. From semi-flexible polymers to membranes: Anomalous diffusion and reptation. *Journal de Physique II*, 7(12):1761–1788, 1997.

[78] T. Munk, F. Hofling, E. Frey, and T. Franosch. Effective perrin theory for the anisotropic diffusion of a strongly hindered rod. *Europhysics Letters*, 85(3):30003, 2009.

[79] S. Ramanathan and D. C. Morse. Simulations of dynamics and viscoelasticity in highly entangled solutions of semiflexible rods. *Physical Review E*, 76:010501, 2007.

[80] I. Szleifer and R. Yerushalmi-Rozen. Polymers and carbon nanotubes - dimensionality, interactions and nanotechnology. *Polymer*, 46(19):7803–7818, 2005.

[81] J. L. Hudson, M. J. Casavant, and J. M. Tour. Water-soluble, exfoliated, nonroping single-wall carbon nanotubes. *Journal of the American Chemical Society*, 126(36):11158–11159, 2004.

[82] C. A. Dyke and J. M. Tour. Unbundled and highly functionalized carbon nanotubes from aqueous reactions. *Nano Letters*, 3(9):1215–1218, 2003.

[83] V. V. Didenko, V. C. Moore, D. S. Baskin, and R. E. Smalley. Visualization of individual single-walled carbon nanotubes by fluorescent polymer wrapping. *Nano Letters*, 5(8):1563–1567, 2005.

[84] S. Badaire, C. Zakri, M. Maugey, A. Derre, J. N. Barisci, G. Wallace, and P. Poulin. Liquid crystals of dna-stabilized carbon nanotubes. *Advanced Materials*, 17(13):1673–1676, 2005.

[85] H. Wang. Dispersing carbon nanotubes using surfactants. *Current Opinion in Colloid and Interface Science*, 14(5):364–371, 2009.

[86] W. Wenseleers, II Vlasov, E. Goovaerts, E. D. Obraztsova, A. S. Lobach, and A. Bouwen. Efficient isolation and solubilization of pristine single-walled nanotubes in bile salt micelles. *Advanced Functional Materials*, 14(11):1105–1112, 2004.

[87] V. C. Moore, M. S. Strano, E. H. Haroz, R. H. Hauge, R. E. Smalley, J. Schmidt, and Y. Talmon. Individually suspended single-walled carbon nanotubes in various surfactants. *Nano Letters*, 3(10):1379–1382, 2003.

[88] P. Cherukuri, C. J. Gannon, T. K. Leeuw, H. K. Schmidt, R. E. Smalley, S. A. Curley, and R. B. Weisman. Mammalian pharmacokinetics of carbon nanotubes using intrinsic near-infrared fluorescence. *Proceedings of the National Academy of Sciences of the United States of America*, 103:18882–18886, 2006.

[89] J. G. Duque, L. Cognet, A. N. G. Parra-Vasquez, N. Nicholas, H. K. Schmidt, and M. Pasquali. Stable luminescence from individual carbon nanotubes in acidic, basic, and biological environments. *Journal of the American Chemical Society*, 130(8):2626–2633, 2008.

[90] R. Wang, P. Cherukuri, J. G. Duque, T. K. Leeuw, M. K. Lackey, C. H. Moran, V. C. Moore, J. L. Conyers, R. E. Smalley, H. K. Schmidt, R. B. Weisman, and P. S. Engel. Swcnt peg-eggs: Single-walled carbon nanotubes in biocompatible shell-crosslinked micelles. *Carbon*, 45:2388–2393, 2007.

[91] Y. J. Kang and T. A. Taton. Micelle-encapsulated carbon nanotubes: A route to

nanotube composites. *Journal of the American Chemical Society*, 125(19):5650–5651, 2003.

[92] C. A. Fustin, V. Abetz, and J. F. Gohy. Triblock terpolymer micelles: A personal outlook. *European Physical Journal E*, 16(3):291–302, 2005.

[93] J. F. Gohy, B. G. G. Lohmeijer, S. K. Varshney, B. Decamps, E. Leroy, S. Boileau, and U. S. Schubert. Stimuli-responsive aqueous micelles from an abc metallo-supramolecular triblock copolymer. *Macromolecules*, 35(26):9748–9755, 2002.

[94] R. B. Weisman. Fluorimetric characterization of single-walled carbon nanotubes. *Analytical and Bioanalytical Chemistry*, 396(3):1015–1023.

[95] M. S. Strano, C. B. Huffman, V. C. Moore, M. J. O'Connell, E. H. Haroz, J. Hubbard, M. Miller, K. Rialon, C. Kittrell, S. Ramesh, R. H. Hauge, and R. E. Smalley. Reversible, band-gap-selective protonation of single-walled carbon nanotubes in solution. *Journal of Physical Chemistry B*, 107(29):6979–6985, 2003.

[96] R. Saito, H. Kotsubo, and K. Ishizu. Synthesis of microspheres with hairy ball structures from poly (styrene-b-2-vinyl pyridine) diblock copolymers. *Polymer*, 33(5):1073–1077, 1992.

[97] W. J. Shin, F. Basarir, T. H. Yoon, and J. S. Lee. Au-coated 3-d nanoporous titania layer prepared using polystyrene-b-poly(2-vinylpyridine) block copolymer nanoparticles. *Langmuir*, 25(6):3344–3348, 2009.